Shifted assembly and function of mSWI/SNF family subcomplexes underlie targetable dependencies in endometrial carcinomas

Jessica D. St. Laurent[1,2,3], Grace D. Xu[1,2,*], Alexander W. Ying[1,2,*], Bengul Gokbayrak[4], Ajinkya Patil[1,2], Joao A. Paulo[5], Kasey S. Cervantes[1,2], Shary Chen[4], William Feng[6], Akshay Sankar[1,2], Daniel D. Samé Guerra[1,2], Jun Qi[6], Dana S. Neel[1], Jason L. Hornick[7], David L. Kolin[7], Steven P. Gygi[5], David G. Hunstman[4], Yemin Wang[4,*], and Cigall Kadoch[1,2,8,9,†]

[1] Department of Pediatric Oncology, Dana-Farber Cancer Institute and Harvard Medical School, Boston, MA, USA 02215
[2] Broad Institute of MIT and Harvard, Cambridge, MA, USA.
[3] Division of Gynecologic Oncology, Department of Obstetrics, Gynecology and Reproductive Biology, Brigham and Women's Hospital, Boston, MA, USA.
[4] Department of Pathology and Laboratory Medicine, University of British Columbia, Vancouver, BC, Canada
[5] Department of Cell Biology, Harvard Medical School, Boston, MA, USA.
[6] Department of Cancer Biology, Dana-Farber Cancer Institute, Boston, MA, USA.
[7] Department of Pathology, Brigham and Women's Hospital and Harvard Medical School, Boston, MA, USA.
[8] Howard Hughes Medical Institute, Chevy Chase, MD, USA.
[9] Lead Contact
* These authors contributed equally to this work.
[†] Correspondence to: Cigall_kadoch@dfci.harvard.edu

[†]Correspondence to:

Cigall Kadoch, Ph.D.
Associate Professor, Department of Pediatric Oncology
Dana-Farber Cancer Institute and Harvard Medical School
Institute Member and Epigenomics Program Co-Director,
Broad Institute of Harvard and MIT
Investigator, Howard Hughes Medical Institute (HHMI)
450 Brookline Avenue, Dana Building D630
Boston, MA 02215
Phone (office): (617)-632-3789
E-mail: Cigall_kadoch@dfci.harvard.edu

Abstract

The mammalian SWI/SNF (mSWI/SNF) family of chromatin remodelers govern cell type-specific chromatin accessibility and gene expression and assemble as three distinct complexes: canonical BAF (cBAF), Polybromo-associated BAF (PBAF), and non-canonical BAF (ncBAF). ARID1A and ARID1B are paralog subunits that specifically nucleate the assembly of cBAF complexes and are frequently co-mutated in highly aggressive dedifferentiated endometrial carcinomas (DDECs). Here, in cellular models and primary human tumors, we find that ARID1A/B deficiency-mediated cBAF loss results in increased ncBAF and PBAF biochemical abundance and chromatin-level functions to maintain the DDEC oncogenic state. Further, treatment with clinical-grade SMARCA4/2 ATPase inhibitors markedly attenuates DDEC cell proliferation and tumor growth in vivo, and synergizes with carboplatin-based chemotherapy to extend survival. These findings reveal the oncogenic contributions of shifted mSWI/SNF family complex abundance and chromatin-level gene regulatory functions and suggest therapeutic utility of mSWI/SNF small molecule inhibitors in DDEC and other cBAF-disrupted cancer types.

Introduction

Genome-wide sequencing efforts performed over the past decade have revealed extensive involvement of chromatin regulatory proteins and protein complexes in human disease[1,2]. Of note, the genes encoding the mammalian SWI/SNF (mSWI/SNF) family of chromatin remodeling complexes are among the most frequently perturbed molecular entities in human cancer and in neurodevelopmental disorders, including several disease pathologies driven uniformly by mSWI/SNF subunit compromise[3–5]. Rare cancers such as malignant rhabdoid tumor, synovial sarcoma, small cell carcinoma of the ovary, hypercalcemic type (SCCOHT), as well as intellectual disability syndromes such as Coffin-Siris syndrome, are considered to be caused by (and in some cases, also diagnosed by) specific mSWI/SNF perturbations[6–12], providing unique windows into the mechanisms by which these complexes control chromatin architecture and regulate gene expression. Studies by our group and others have leveraged such settings to inform subunit-specific contributions to mSWI/SNF activity, delineate subunit biochemical assembly and structural relationships, and inform unique vulnerabilities that can be accompanied by novel therapeutic approaches[13–18].

Recently, targeted sequencing and immunohistochemical characterization of a uniquely aggressive form of endometrial cancer, dedifferentiated/undifferentiated endometrial carcinoma (DDEC/UEC), revealed a high prevalence of mSWI/SNF perturbations in over 70% of cases[19–21], suggesting mSWI/SNF perturbation as a key molecular event underlying dedifferentiation. DDEC/UEC is an epithelial malignancy comprising an undifferentiated carcinoma that arises in the background of a well-differentiated endometrioid carcinoma[20]. Among mSWI/SNF mutations, concomitant mutation of ARID1A and ARID1B subunits is most common, with SMARCA4 and SMARCB1 as other frequently disrupted subunit genes (**Figure 1A, S1A-D, Table S1**) [22]. In many cases, loss of both ARID1A and ARID1B expression is observed in the undifferentiated component whereas the corresponding differentiated component shows intact expression of ARID1B[19,22]. Furthermore, DDEC cases can exhibit mutations in *POLE* and *TP53* (**Figure S1A-C**), highlighting that mSWI/SNF-mutated DDEC can arise in all characterized mutational backgrounds of endometrial carcinoma[21,23,24]. Of note, compared to mSWI/SNF-intact DDEC cases, ARID1A/B-dual mutated cases result in significantly shorter overall survival (~4 months versus ~36 months) and increased resistance to conventional chemotherapy with advanced stage disease[19,21,22]. Taken together, these studies underscore that concomitant ARID1A/B loss defines a highly aggressive group of undifferentiated endometrial cancers characterized by rapid disease progression and insensitivity to conventional platinum and taxane-based chemotherapy, highlighting a major unmet need to understand the disease biology and define new therapeutic opportunities.

Here we define the biochemical and chromatin regulatory mechanisms underlying ARID1A/B dual-deficient DDEC cancers, unmasking new therapeutic opportunities. We find that complete cBAF disruption via ARID1A/B dual loss drives increased relative abundance of ncBAF and PBAF subcomplexes of the mSWI/SNF family in both cellular models and DDEC primary tumors, resulting in enhanced gene regulatory functions of these complexes at both enhancers and promoters genome-wide. Notably, increased ncBAF and PBAF chromatin remodeling activities support a gene expression network conducive to hyperproliferation and loss of differentiation. This effect is attenuated by either ectopic restoration of ARID1A/B or by inhibition of mSWI/SNF catalytic activity with clinical-grade small molecule inhibitors in both cell culture and in vivo tumor model systems. Taken together, these findings define the molecular underpinnings of one of the most aggressive and intractable human cancers and inform new potential therapeutic approaches for a tumor type sorely lacking treatment options.

Results

Human cell lines and primary tumors with dual ARID1A/B loss exhibit increased residual mSWI/SNF complex protein abundance

To characterize the protein-level features of mSWI/SNF complex componentry in endometrial carcinomas, we first curated tumor-derived cell lines bearing wild-type (WT) mSWI/SNF gene status, those with mutations only in ARID1A, and those characterized by dual-loss of ARID1A and ARID1B, isolated nuclear material and performed immunoblot analyses for mSWI/SNF family subunits (**Figure 1B-C, S1E, Table S2**). Notably, among all endometrial lines, >55% are scored to contain loss-of-function mutations in ARID1A, consistent with high percentages found in human tumors[22,25,26]. Notably, in DDEC tumors, while cBAF-specific ARID1A/B subunits were entirely absent, we found that ncBAF-specific subunits, BRD9, GLTSCR1, and GLTSCR1L as well as PBAF subunits, ARID2 and BRD7, were increased in protein-level abundance in these cell lines (**Figure 1C-D**). To further examine this, we subjected nuclear extracts of an mSWI/SNF-intact cell line, KLE, and the ARID1A/B-dual deficient cell line, VOA1066, to density sedimentation analyses using 10-30% glycerol gradients (**Figure 1E**). Notably, subunits including SMARCC1 and SMARCD1, core module subunits that can nucleate both ncBAF and cBAF complexes, exhibited clear shifts toward the lower (fractions 8-11) and upper (fractions 16-18) molecular weight fractions in the VOA1066 cell line relative to the KLE cell line (**Figure 1E**). Further, we noted increases in BRD9 and GLTSCR1/1L ncBAF subunit intensities (relative to total input) in fractions 6-11 and PBAF-associated PBRM1 intensities in the dual-deficient VOA1066 cell line relative to the KLE mSWI/SNF-intact cell line (**Figure 1E**). Finally, we performed comprehensive immunohistochemical profiling on a collection of n=109 primary human DDEC tumors bearing both undifferentiated (n=109) and well-differentiated (n=69) regions (**Figure 1G, S1G**). Notably, we found that immunostaining of GLTSCR1, the nucleating member of ncBAF complexes, was significantly elevated in de-differentiated tumor compartments, with similar intensities of the ATPase subunit, SMARCA4 (**Figure 1H**). Together, these data present the observation that as a result of cBAF disruption via ARID1A/B dual loss, remaining mSWI/SNF subcomplexes exhibit altered subunit protein-level abundance in both cellular models and primary human tumors.

ARID1A restoration results in biochemical and genome-wide rebalance of mSWI/SNF complexes

To determine whether the above observations in cell lines and primary tumors were specifically due to the loss of the ARID1A/B subunits, we next generated a system for the restoration of full-length WT ARID1A in DDEC cell lines (**Figure 2A**). Notably, we found that doxycycline-induced ARID1A rescue into both VOA1066 and AN3CA cells resulted in reduced nuclear protein levels of ncBAF (BRD9 and GLTSCR1 (in VOA1066) as well as PBAF (ARID2) components (**Figure 2B**). Importantly, density sedimentation analyses performed on both VOA1066 and AN3CA cell lines with and without Dox-mediated ARID1A rescue for 72 hours confirmed a clear redistribution of ncBAF-cBAF shared core module subunits, such as SMARCC1 and SMARCD1, as well as ATPase subunits SMARCA4 and SMARCA2 (**Figure 2C, S2A**). Quantitative tandem mass tag (TMT) mass-spectrometry-based proteomic experiments performed on total cell lysates confirmed these findings quantitatively in both DDEC cell lines, revealing significant changes in subunit protein abundance of ncBAF and PBAF subunits and restoration of cBAF abundance following ARID1A rescue (**Figure 2D-E, S2B-D, Table S3**). Importantly, shifted complex assembly following ARID1A reintroduction was accompanied by significant reductions in proliferation of AN3CA and VOA1066 cell lines coupled with altered morphology suggestive of endometrial differentiation in culture (**Figure 2F, S2E-G**).

Given these biochemical changes and their associated impact on cell proliferation, we next sought to determine the chromatin-level changes in mSWI/SNF complex occupancy following ARID1A rescue in DDEC cell lines (**Figure 2A**). We began by profiling the genome-wide occupancy distribution

of mSWI/SNF complexes marked by SMARCA4 (present in all mSWI/SNF subcomplexes), and found that ARID1A restoration led to a large number of gained sites genome-wide (n=36415), as well as a smaller number of sites with retained occupancy (n=13573), and lost or reduced occupancy (n=5637) in AN3CA cells (**Figure 2G, Figure S2H-I**). Sites with gained mSWI/SNF complex targeting corresponded largely to restored cBAF complex occupancy as exhibited by strong overlap with ARID1A, the SS18 subunit, as well as substantial increases in the H3K27Ac mark known to correspond to active enhancer and promoter regions[27,28] (**Figure 2G**). These gained sites also exhibited strong increases in chromatin accessibility as profiled via ATAC-seq (**Figure 2H**). To further understand the features of these sites, we performed distance-to-TSS and HOMER motif enrichment analyses (**Figure 2H, S2I**). Notably, we found that SMARCA4-gained sites were largely TSS-distal, consistent with rescue of cBAF assembly and localization to distal enhancer sites[14,17] (**Figure 2H**) and motifs enriched over gained sites in AN3CA cells included those corresponding to cBAF-associated motifs such as Fos, Jun, AP-1, and ATF3 bZIP transcription factors (TFs)[29,30] (**Figure 2H**). Similar results were obtained in the VOA1066 cell line (**Figure S2H-J**). Sites with gained mSWI/SNF occupancy were observed over loci such as *KRT7 and CLDN2* (**Figure 2I**). In parallel, we performed ATAC-seq experiments and analyses to define the changes in genome-wide chromatin accessibility. In both AN3CA and VOA1066 cell lines, accessibility was gained across a large number of sites upon ARID1A rescue, corresponding to increases in cBAF complex targeting to distal regions (**Figure 2G, S2K-L**). These data are indicative of the role for ARID1A and hence cBAF complexes in restoring open chromatin architecture and subsequent activation of genes such as lineage markers in DDEC.

In contrast, however, we noted that sites that exhibited reductions in SMARCA4 occupancy, as well as those with retained occupancy following ARID1A restoration correlated with sites showing strong reductions in ncBAF occupancy, as indicated by BRD9 and GLTSCR1 ChIP-seq (**Figure 2G, J**). Intriguingly, these sites were not accompanied by significant changes in accessibility (**Figure 2G, K, S2M**), consistent with prior studies indicating a lesser role for ncBAF complexes in chromatin accessibility generation relative to cBAF[17,18]. Correspondingly, SMARCA4-marked lost sites upon ARID1A restoration in DDEC cell lines were skewed toward promoter-proximal locations and exhibited strong enrichment for CTCF and BORIS (CTCF-like) Zf TF motifs known to be targeted by ncBAF complexes[17] (**Figure 2H, S2J**). We next analyzed ChIP-seq profiles for ncBAF components, BRD9 and GLTSCR1, to evaluate the occupancy of this mSWI/SNF family complex over sites of altered chromatin accessibility. Notably, we identified that upon ARID1A rescue, BRD9 and GLTSCR1 occupancy was substantially reduced, especially over sites of both retained and lost chromatin accessibility (**Figure 2J-K, S2M**). This is exemplified over the *E2F2* and *KCNG4* loci (**Figure 2L**). Finally, we examined the PBAF-specific subunit, PBRM1, finding that PBAF complexes mainly localized to retained sites in either empty or ARID1A rescue conditions, albeit with minimal changes to occupancy levels over promoters (**Figure S2N-O**).

Taken together, these data demonstrate marked changes in both protein-level abundance and genomic binding and activity of mSWI/SNF family complexes, specifically ncBAF and PBAF complexes, that are controlled by cBAF assembly in DDEC cells.

ARID1A restoration leads to differentiation and loss of oncogenic programs in DDEC cells

We next sought to define the impact of ARID1A restoration on gene expression via RNA-seq performed in DDEC cell line contexts. Globally, upon restoration of ARID1A in both VOA1066 and AN3CA cell lines for 72 hours, we identified both gains and losses in gene expression, with ~4-5-fold more genes upregulated than downregulated (**Figure 3A, S3A**). These data align with the outsized gains in chromatin accessibility observed in both cellular model systems (**Figure 2G, S2L**). Across both DDEC cell lines, upregulated genes corresponded to those central to hormone response (estrogen and androgen),

inflammation (inflammatory response, IFNalpha/gamma response, TNFa and TGFb), as well as apoptosis (apoptosis, P53 pathway) (**Figure 3B, S3B-D**). Consistent with the antiproliferative impact of ARID1A restoration (**Figure 2F, S2E-G**), gene expression pathways most strongly downregulated included those of MYC targets, G2M checkpoint, mitotic spindle, E2F targets and mTORC signaling (**Figure 3B, S3B-D**). These results were consistent between both DDEC cell lines, with concordantly upregulated genes such as *PDGFR*, *VASN* and *IL17RD* and downregulated genes such as *FOSL1*, *UBR7*, and *BCL2L2* (**Figure 3A-B, S3E-F**). Comparative analyses of gene expression (RNA-seq) changes and whole-cell protein abundance (TMT-mass spectrometry) identified genes/proteins whose changes overlapped. Notably, proteins associated with cell-cell adhesion, tissue-specific cell differentiation, and apoptosis/cell death were upregulated, while those involved in cell cycle, DNA repair and DNA replication were downregulated at both the RNA and protein levels (**Figure 3C**). Together, these concordant RNA and protein-level data emphasize the impact of ARID1A restoration, and consequently cBAF complex reconstitution, in DDEC cell line models.

We next sought to integrate these data with mSWI/SNF chromatin occupancy studies to define putative direct target functions of cBAF loss and ncBAF/PBAF complex gains and their shifted targeting genome-wide. Indeed, among ARID1A-mediated downregulated genes defined by RNA-seq experiments, ~48% and ~37% were genes near sites of lost ncBAF (BRD9-/ GLTSCR1-shared sites) targeting in AN3CA and VOA1066 cells, respectively (**Figure 3D**). Approximately 26% and 51% of upregulated genes were those nearby sites of increased cBAF chromatin occupancy and accessibility (HA-ARID1A-/SMARCA4-shared sites) in AN3CA and VOA1066 cells, respectively (**Figure 3D**). As examples, we defined increased cBAF targeting, accessibility and gene expression at the *IL7R*, *NRP1*, and *KRT7* genes and concomitant decreased ncBAF targeting and gene expression, coupled with more minor changes in accessibility over the *E2F2*, *WNT10B* and *INHBA* genes in AN3CA cells (**Figure 3E, S3E-F**). This is exemplified at the *KRT7* and *E2F2* loci, respectively (**Figure 3F**, **S3H**). Together, these data are consistent with DDEC tumor cell redifferentiation down the endometrial lineage, regain of factors necessary for endometrial cell function, and reactivation of pathways such as hormone response. In parallel, examination of genes significantly attenuated in expression upon the restoration of ARID1A in DDEC cell lines were those nearest sites of reduced ncBAF complex occupancy and accessibility, including those genes associated with tumor cell invasion, EMT, DNA repair and cell proliferation (**Figure 3D-F, S3F-H**).

Given that DDEC tumors exhibit concomitant loss of ARID1A and ARID1B paralog subunits of cBAF complexes, we next sought to define the impact of restoration of each paralog in isolation and together (**Figure 3G-H, S3I-J**). Following confirmation of protein expression of HA-tagged ARID1A, ARID1B, and both paralogs together in AN3CA cells, we performed RNA-seq and ATAC-seq studies to define the shared and disparate gene regulatory and chromatin accessibility profiles, respectively. Intriguingly, over two thirds (67.3%) of ARID1A-mediated upregulated genes were also upregulated by restoration of ARID1B; ARID1B, however, resulted in more upregulated genes than ARID1A (n=1720 versus n=1187 for ARID1A rescue) (**Figure 3I-J, left**). For downregulated genes, ARID1B also induced higher numbers of downregulated of genes relative to ARID1A (n=1136 versus n=274 for ARID1A) (**Figure S3K**). Notably, a collection of 589 genes were uniquely upregulated and 622 genes uniquely downregulated only with the rescue of both ARID1A and ARID1B rather than either alone (**Figure 3J left, S3K**). To define whether these were upregulated or downregulated marginally by either alone and more significantly by ARID1A/B, or whether such genes were only activated/repressed when ARID1A/B were co-present in cells, we performed clustering analyses. These genes, deemed 'synergistic genes', included those such as *DUSP10*, *RARS2*, and *ANKRD11* as upregulated genes and *EBP*, *GEMIN4*, *NONO* and *SP1* as downregulated genes (**Figure 3K)**, which also exhibited concordant changes in accessibility as assessed by ATAC-seq and corresponded to adipogenesis and FLT3 signaling pathways (upregulated) and JAK2 targets, fatty acid metabolism, and endocrine therapy resistance

(downregulated) (**Figure 3K, S3L**). The gene regulatory impact of ARID1A or ARID1B or both paralogs (majority of genes) included restoration of estradiol response, silencing of proliferative pathways and induction of senescence pathways, upregulation of SMARCA4 target genes, and downregulation of G2/M and DNA replication signatures (**Figure S3L**). Of note, specific TF target genes (i.e. STAT3 targets, HOXA5 targets, FOXA2 targets, and AP1 pathway targets were only upregulated significantly with restoration of ARID1B or both paralogs, but not ARID1A alone (**Figure S3L**). Notably, sites of increased accessibility were largely conserved between single ARID1 paralogs and their concomitant expression, with only 468 sites among >54,000 total sites showing increased accessibility only in the dual rescue condition (+ARID1A/+ARID1B) (**Figure 3J, right**). Notably, these 468 sites were largely those correlating with synergistic genes identified that required both paralogs for activation (**Figure 3K**).

Finally, given these results coupled with the fact that the highest ncBAF and PBAF protein levels were observed in the undifferentiated compartments of DDEC tumors, we next isolated n= 4 primary human ARID1A/B dual-deficient DDEC tumors and performed laser capture microdissection (LCM) to isolate RNA from well-differentiated (WD) and undifferentiated (UD) compartments of DDEC tumors and normal tissue (**Figure 3L, Table S4**). Differential gene expression results performed between UD and WD regions indicated genes such as *ALDH1A1*, *TBX15*, and *MFAP5* as significantly upregulated genes in DDEC regions of all tumors, with genes such as *SOX14*, *CLDN2*, *CLCL14* and transporter genes *SLC16A12* and *SLC47A1* as upregulated in the WEC regions (**Figure 3M**). Comparing gene sets of UD and WD regions of endometrial tumors, we identified that genes corresponding to hormone response (estrogen response early/late genes) as significantly upregulated in the WD regions, while genes corresponding to DNA repair, MYC targets, EMT, cell cycle and IFNa/TNFa signaling were upregulated in the DD compartments (**Figure 3M-N**). Importantly, comparing gene sets of genes differentially expressed in the UD and WD components of primary tumors, those in normal endometrium, and those in cell line models, VOA1066 and AN3CA, we identified several clusters of genes that exhibited similar gene expression profiles and that were impacted by ARID1A rescue (**Figure 3O, S3M-N**). Together, these results highlight the impact of cBAF restoration on endometrial carcinoma cell gene expression programs and underscore the utility of DDEC cellular models in mirroring the expression of primary tumors.

CRISPR-mediated disruption of residual ncBAF and PBAF complexes attenuates cell proliferation and oncogenic gene signatures in DDEC

We next sought to determine the impact of mSWI/SNF complex disruption on DDEC cell line proliferation. To do this, we generated AN3CA and VOA1066 cell lines with inducible shRNAs targeting either BRD9 (ncBAF) or ARID2 (PBAF), relative to a scrambled control, and assessed cell growth using colony formation assays at 6 days post induction (**Figure 4A**). Indeed, suppression of either BRD9 and ARID2 levels resulted in significant reduction in proliferation of both AN3CA and VOA1066 cell lines (**Figure 4A-B, S4A-C).** Further, we evaluated pooled CRISPR knockout (KO) of ARID2, GLTSCR1, GLTSCR1L, SMARCA4 (BRG1) and SMARCA2 (BRM) on AN3CA cell viability in culture, finding that each resulted in suppression of AN3CA proliferation (**Figure S4D-E**).

We next aimed to define whether the dual loss of ARID1A and ARID1B accentuated the sensitivity of DDEC cell lines to the depletion of mSWI/SNF components, specifically, those corresponding to residual cBAF and PBAF complexes. To do this, we used the ARID1A-deficient HEC1B endometrial cancer cell line in which we either treated with control CRISPR gRNAs or those targeting ARID1B, generating a dual ARID1A/ARID1B-deficient HEC1B cell line (**Figure 4C**). Using genome-wide CRISPR/cas9 screens in both cell settings, we defined genes that selectively impacted the proliferation of endometrial cancer cells lacking both ARID1 cBAF paralogs (**Figure 4D, S4F-G, Table S5**). Notably, examination of all mSWI/SNF genes indicated increased dependencies on PBAF components PBRM1

and ARID2, as well as ncBAF components GLTSCR1L and SMARCD1 in ARID1A/ARID1B dual deficient HEC1B cells (**Figure 4E**). We validated these results using colony formation assays (**Figure S4H-J**). Interestingly, depletion of BRD9 component of ncBAF resulted in proliferative attenuation of both HEC1B parental control (ARID1A-deficient) and HEC1B-ARID1B KO cells (**Figure S4I**), consistent with results of the CRISPR screen indicating significant depletion scores for ncBAF components SMARCD1 and BRD9 in both conditions (**Figure 4E**). In parallel, we evaluated all selective dependencies identified in the genome-scale CRISPR screen highlighting those that uniquely scored as significant in the HEC1B-ARID1B KO setting. Notably, we identified several hits that scored as selective dependencies in the dual ARID1 paralog-deficient setting (**Figure 4F**). These included genes such as *POLA2*, *RAPTOR*, and *NUP50*, corresponding to pathways such as MYC targets, G2/M checkpoint, DNA replication and undifferentiated cancer signatures (**Figure 4F-G**). To dissect these and define which dependencies may result from heightened ncBAF and PBAF mediated gene regulation, we identified the top 20 dependencies specific to the HEC1B ARID1B KO setting and defined their changes in gene expression in AN3CA and VOA1066 DDEC cell lines upon ARID1A restoration. Importantly, using this approach, we were able to define several of these top dependencies as ARID1A/ARID1B (cBAF) loss dependent genes (**Figure 4H, S3K**). Further, we sought to evaluate the overlap between top dependencies in HEC1B WT and ARID1B KO settings and those genes in DDEC cell lines AN3CA and VOA1066 impacted by SMARCA4/2 ATPase inhibition using Cmp14[31]. Notably, we identified several gene dependencies in the HEC1B ARID1A/ARID1B dual loss condition that are downregulated upon mSWI/SNF ATPase inhibition in AN3CA and VOA1066 cell lines, including *KANK3*, *KANK4*, *KLF15*, *MYO5C* and *STAP2* (**Figure 4I**).

Finally, to assess the functional dependence of endometrial cell lines of different statuses with respect to ARID1A/B disruption, we next identified a range of cancer cell lines, including endometrial lines, that are ARID1A/B dual-deficient, ARID1A-deficient and ARID1A/ARID1B-intact. In line with our experimental findings, cell lines with either ARID1A-only or dual ARID1A/ARID1B losses exhibited increased reliance on the ncBAF component, BRD9 and the PBAF component ARID2, as well as to an extent, SMARCD1 (**Figure 4J**).

Pharmacologic targeting of residual mSWI/SNF complexes in DDEC inhibits cell proliferation and cancer-associated accessibility and gene expression

We next aimed to define the utility of small molecule inhibitors of mSWI/SNF complex ATPase activity, including Cmp14[31] as well as dBRD9-A, a small molecule degrader of the BRD9 component of ncBAF[17,32] (**Figure 5A**). Treatment with either Cmp14 or dBRD9-A (500nM or 1μM, respectively) for 15 days resulted in marked attenuation in cell proliferation of ARID1A/B dual-deficient DDEC cells in culture (**Figure 5B, S5A**). Cmp14-mediated ATPase inhibition resulted in the most complete attenuation of proliferation in both cell lines (**Figure 5B, S5A**). To understand the gene regulatory changes underlying these results, we next performed RNA-seq experiments in both VOA1066 and AN3CA cells treated with either Cmp14 or dBRD9-A for 72 hours. Principal component analyses revealed separation relative to DMSO control, with greatest variance in the Cmp14-treated condition in both DDEC cell lines (**Figure S5B-C**). Genes downregulated by both Cmp14 and dBRD9-A included those corresponding to stem cell signatures, SMARCA4 target genes, EMT, and MYC targets, tumor invasiveness and TGFB1 signatures (**Figure 5D, S5D-E**). Upregulated gene sets included EZH2 targets, estrogen response, E2F targets, and cholesterol biosynthesis (**Figure 5D, S5D-E**). Intriguingly, the majority of pathways identified were impacted similarly by each small molecule treatment (Cmp14 and dBRD9-A), with some pathways, particularly downregulated pathways, more strongly impacted by Cmp14, as predicted by PCA analyses (**Figure 5D, S5E**). We identified several shared downregulated genes including *SERPINE1*, *LIPG*, *NDRG1*, and *EMP1*, among others (**Figure 5E, S5F-G**). Notably, several of these were direct targets of BRD9-containing ncBAF complexes in both VOA1066 and AN3CA cells (**Figure 5F, S5H**).

We next performed ATAC-seq in the setting of both treatment conditions. Notably, major changes were observed with the Cmp14 treatments in both cell lines whereas dBRD9-A treatment resulted in less substantial changes in accessibility (**Figure 5G, S5I-M**). Of note, Cmp14, targets the ATPase activity of both ncBAF and PBAF complexes, and in concordance, resulted in both gains and losses in accessibility (**Figure S5I,L).** Specifically, over sites with the most marked reduction in accessibility with Cmp14, accessibility was only modestly impacted with dBRD9-A, yet gave rise to similar decreases in target gene expression (**Figure 5G**). Examples of genes with concordant changes in accessibility and gene expression upon Cmp14 and to more modest extents, dBRD9-A, (i.e. those with decreased accessibility and decreased expression) included *RTL1*, *SERPINE1*, *NUPR1*, *EMP1*, and *S100A4* among others (**Figure 5H, 5F**) and corresponded to EMT and stemness signatures (**Figure S5N**).

Finally, we evaluated the response of HEC1B ARID1A-deficient and ARID1A/B-dual deficient (HEC1B ARID1B KO) model systems to FHD-286, a clinical grade inhibitor of SMARCA4/2 ATPase activity.[33–35] Indeed, treatment of the ARID1A/B-dual deficient HEC1B cells resulted in greater antiproliferative impact, as assessed by colony formation assays (**Figure S5O-P**). Together, these data implicate the potential utility of both ATPase inhibitors and BRD9 degraders as molecules that attenuate the oncogenic chromatin and gene regulatory profiles of DDEC tumors.

Pharmacologic mSWI/SNF complex inhibition attenuates tumor growth and potentiates survival in vivo

Lastly, we sought to determine the impact of mSWI/SNF complex inhibition on DDEC tumor growth in vivo using both cell line-derived xenograft (CDX) and patient-derived xenograft (PDX) model systems. Specifically, we established subcutaneous tumor models of the VOA1066 cell line (cell line xenograft (CDX)) and a novel PDX, XVOA14590, derived from a human DDEC primary tumor lacking both ARID1A and ARID1B expression (**Figure S6A**). NRG mice were implanted with 25mg of homogenized tumor and allowed to grow to ~75mm^3 prior to start of treatment. Specifically, we evaluated either Cmp14 SMARCA4/2 ATPase inhibitor (25mg/kg dosed QD as IP injections) or the BRD9 degrader, dBRD9-A (50mg/kg, dosed QD as IP injections) (**Figure 6A**). Treatment of XVOA14590 PDX with either Cmp14 or dBRD9-A resulted in statistically significant reductions in tumor volume by the study endpoint of 16 days, with average tumor volume for the vehicle control reaching the endpoint of 1500m^3, while volumes for Cmp14 and dBRD9-A treatment conditions averaged 800mm^3 and 450mm^3 respectively (**Figure 6B, S6B-D**). Tumor burden (relative to % body weight) was also attenuated in a statistically significant manner by both dBRD9-A and Cmp14 treatment, with Cmp14 achieving the largest effect (**Figure 6C**). Degradation of BRD9 was confirmed in vivo using immunoblot performed on tumors collected at the study endpoint (Day 16 post-treatment) (**Figure S6D**). In addition, treatment of VOA1066 CDX with Cmp14 (20 mg/kg, QD, oral) led to significant decrease of both tumor volume and final tumor weight (**Figure 6F, S6H**).

To define the similar and distinct impacts of each treatment in vivo, we isolated RNA from n= 6 XVOA14590 PDX tumors at Day 16 post treatment (study endpoint and performed RNA-seq gene expression analyses. Principal component analyses (PCAs) indicated treatment-dependent shifts in gene expression relative to vehicle control and confirmed experimental replicate concordance in vivo (**Figure S6E, n=6**). Notably, treatment of either Cmp14 or dBRD9-A, particularly Cmp14, led to significant suppression of several key pathways, including cancer progenitor signatures, stemness signatures, TGFB targets, SOX4 targets (C2 pathways) as well as early estrogen response, EMT and inflammatory response pathways (i.e. TNFalpha, interferon alpha, and others) were downregulated upon treatment with either Cmp14 or dBRD9-A or both (**Figure 6D, S6F-G**). We identified additional pathways that were only upregulated and downregulated in the setting of Cmp14 treatment and not dBRD9-A,

such as those corresponding to differentiation and restoration of P53/senescence targets (upregulated), SMARCA4 targets (downregulated) and multicancer invasiveness (downregulated), in part explaining the greater impact observed with ATPase inhibition relative to dBRD9-A treatment with respect to tumor growth in vivo (**Figure 6D, S6F-G**). Of note, in comparing the impact of Cmp14 and dBRD9-A treatments in this primary human tumor-derived DDEC PDX with our results in VOA1066 and AN3CA DDEC cell lines, we identified a collection of genes that were concordantly up- and down-regulated in 2D culture in VOA1066 and AN3CA cell line models as well as in the PDX XVOA14590 model in vivo (**Figure 6E**). Further, Cmp14 treatment exhibited a similar anti-tumoral effect in the VOA1066 CDX model in vivo (**Figure 6F, S6I**).

In parallel, we evaluated the impact of FHD-286, a clinical-grade small molecule inhibitor of the SMARCA4/SMARCA2 ATPases currently under evaluation in Phase I clinical studies (i.e. NCT04891757) [36]. Notably, treatment with FHD-286 (1.5mg/kg, QD) for 25 days also attenuated tumor growth in vivo of the VOA1066 CDX model modified with GFP-luciferase (**Figure 6G, S6H**). Further, given the efficacy of standard-of-care carboplatin across endometrial carcinoma subtypes and the observed DNA replication and repair pathways we identified as altered upon mSWI/SNF perturbation (specifically with SMARCA4/2 ATPase inhibition, and to an extent, BRD9 degradation) in DDEC, we sought to define whether treatment with FHD-286 would potentiate the activity of carboplatin on DDEC cell line growth in culture and tumor growth in vivo (**Figure 6H**). Indeed, in cell culture systems, both ARID1A/ARID1B dual-deficient (i.e. VOA1066) as well as ARID1A-deficient models (i.e. RL95-2, SNGM) cell lines exhibited synergistic responses in the setting of combined FHD-286 and carboplatin (**Figure S6I**). We thus evaluated the potential for combination FHD-286 plus carboplatin benefit in vivo using the XVOA14590 PDX and VOA1066 CDX model systems (**Figure 6H**). Importantly, we observed significant potentiation in overall mouse survival relative to either single agent alone, without meaningful changes in mouse body weight (**Figure 6I-J, Figure S6J-K**). Together, these findings highlight the potential clinical utility of FHD-286 either alone or in combination with anti-proliferative chemotherapeutics such as carboplatin in DDEC.

Discussion

Dedifferentiated endometrial carcinoma is characterized by the frequent disruption in mSWI/SNF genes, and remains a highly aggressive tumor type with poor overall survival and limited treatment options beyond conventional chemotherapy. First-line standard of care treatment for these tumors include cytotoxic chemotherapy such as carboplatin and paclitaxel with immunotherapy being increasingly incorporated into treatment regimens, albeit with limited success and limited biomarkers capable of identifying patients with increased likelihood of benefit[19,37,38]. As such, there remains a high unmet medical need to identify new therapeutic opportunities that, either alone or in combination, can attenuate or inhibit the growth of DDEC tumors. Here, our study focuses on the immediate biochemical ramifications of dual loss of the ARID1A and ARID1B paralogs that are required for cBAF assembly[15]. We find that, without these two subunits, only residual ncBAF and PBAF mSWI/SNF remodeler subcomplexes exist on chromatin, enhancing their function via both increased stoichiometric abundance and increased remodeling activities toward oncogenic benefit. These enhanced functions lead to activities that uphold the cancer state, including loss of lineage-associated proteins routinely profiled by IHC in these tumors including cytokeratins that appear to be controlled and maintained by cBAF.

Building on prior work establishing ARID1A as a tumor suppressor in the endometrium and mSWI/SNF involvement more broadly[39–42], here we demonstrate its critical role in epithelial lineage commitment and differentiation. Mechanistically, ARID1 expression in DDEC tumor cell lines promotes cBAF reassembly and binding at distal enhancers associated with epithelial differentiation and estrogen signaling

pathways. Further, here, we directly compare the roles for ARID1A, ARID1B and both (ARID1A+ARID1B) in the AN3CA DDEC cell line, gaining new insights into how these two paralogs shape chromatin accessibility and transcriptional landscapes (Figure 3). Of note, our data suggests substantial functional redundancy in the cellular context of endometrial carcinoma, with the majority of gained accessible sites and upregulated genes shared upon ARID1A and ARID1B reintroduction. However, we also identify gene sets relevant to oncogenic maintenance in DDEC that can only be rescued by ARID1B reexpression or the combination of ARID1A/B, opening new opportunities to define mechanisms of paralogs. Notably, cBAF restoration, regardless of whether mediated by ARID1A or ARID1B, leads to altered cell morphology and cytokeratin expression, phenocopying well-differentiated endometrial carcinoma. These findings collectively establish cBAF as a pivotal regulator of epithelial lineage commitment, potentially representing a broader mechanism by which cBAF activities influence cancer cell fate.

While the role for cBAF in regulating chromatin accessibility, particularly at distal enhancers, is well established,[13,14,18,43] the specific functions of ncBAF and PBAF are less well understood. Our group has previously reported increased ncBAF abundance and activity in other cBAF-mutated cancer contexts including SMARCB1-deficient malignant rhabdoid tumor, and SMARCE1-deficient clear cell meningioma.[18,43] Here, our work demonstrates the intriguing persistence of both ncBAF and PBAF at key loci associated with cell survival and proliferation in the absence of cBAF. Additionally, we identified a set of TSS-proximal sites that correlate with upregulated genes encompassing key oncogenic driver pathways, including MYC and progenitor and stemness signatures. ncBAF and PBAF complexes are required for maintenance of ARID1A/B dual-deficient cells, a therapeutic vulnerability that we validate both genetically and with pharmacologic small molecule inhibitors. In contrast to SMARCA4/SMARCA2-deficient cancers such as SCCOHT, the majority of ARID1A/ARID1B-mutant DDECs retain SMARCA4 and/or SMARCA2 expression (Figure 1), making them amenable to treatment with SMARCA4/2 ATPase inhibitors such as FHD-286. In DDEC, this therapeutic strategy proved more effective than solely targeting ncBAF with BRD9 degradation in vivo, suggesting either that the ATPase activity of both ncBAF and PBAF contribute to oncogenic maintenance, or, that BRD9 degradation is insufficient to attenuate ncBAF-mediated functions in this context.

In contrast to other studies,[44] we do not find that PBAF complex functions are reduced or assembly is altered; indeed, based on these studies and assembly work[15], the cBAF assembly pathway is separate and distinct from that of PBAF and ncBAF, connected only by the fact that increased PBAF and ncBAF are formed when cores can no longer nucleate cBAF complexes in the absence of ARID1A/B. Of note, dual loss of the ARID1A/B paralogs also occurs in dedifferentiated cancers beyond DDEC including 4% of gastric and 1-2% of liver cancers.[45–48], suggesting the relevance of our findings to a meaningful number of cancer cases. Further, dual loss ARID1A/B in the setting of the liver suggest similar levels of aggressiveness, enhanced dedifferentiation and impaired liver function[44]; based on our mechanistic findings, FHD-286 alone or in combination with chemotherapy may represent a viable therapeutic opportunity for these cancers warranting clinical investigation.

Finally, our findings underscore the importance of incorporating genetic profiling (e.g. ARID1A/B mutational status) in the evaluation of endometrial carcinomas and during DDEC classification. Defining DDEC by histologic subtype alone currently excludes patients from most clinical trials in gynecologic oncology clinical trials, including those incorporating mSWI/SNF-mutated tumors. Our data argue that mSWI/SNF-mutant DDEC lies within a spectrum of cBAF-mutated endometrial carcinomas that can be characterized by the relative abundance of remaining functional cBAF complexes, which constitutes the mechanisms and targetable dependencies defined herein. Further studies will be needed to define the

consequences of specific 'doses' of remaining cBAF abundance in ARID1A-mutant endometrial carcinomas.

Acknowledgements
We thank all of the members of the Kadoch Laboratory and Wang/Huntsman Laboratories for assistance and discussion throughout the duration of this project. Specifically, we thank Dr. Siddhant Jain for assistance with ARID1A piggybac construct cloning, Eunice Li for isogenic cell line generation, as well as Chae Young Shin and Lien Hoang for assistance with DDEC microdissection. We also thank Zach Herbert, Maura Sullivan and Rachel Garuti of the DFCI Molecular Biology Core Facility (MBCF) for help with high-throughput sequencing. J.S.L. is supported by the NIH RDSP (Grant #K12-HD000849-37) and the GOG foundation. This work was supported in part by an NIH DP2 New Innovator Award (C.K.) and the Howard Hughes Medical Institute (HHMI), Canadian Institute of Health Research (CIHR) grant PJT-462168 (Y.W.), Terry Fox New Frontiers Program Project Grants (#1116, Y.W.; #1082, D.G.H). Y.W. is a recipient of the North Family Health Research Award. D.G.H. is supported by a Canada Research Chair in Molecular and Genomic Pathology. The authors also thank the Molecular Biology Core Facility (MBCF) at the DFCI (especially Zach Herbert and Maura Sullivan). We also appreciate the generous support from the British Columbia Cancer Foundation and the VGH/UBC Hospital Foundation.

Conflict of Interest Statement
C.K. is the Scientific Founder, Scientific Advisor to the Board of Directors, Scientific Advisory Board member, shareholder, and consultant for Foghorn Therapeutics, Inc. (Cambridge, MA), serves on the Scientific Advisory Boards of Nereid Therapeutics and is a consultant for Cell Signaling Technologies and Google Ventures. C.K. is also a member of the *Molecular Cell* and *Cell Chemical Biology* Editorial Boards. J.S.L is a shareholder for AI Proteins Inc. (Boston, MA). The other authors declare no competing interests.

Author Contributions
J.S.L: Conceptualization, methodology, validation, formal analysis, investigation, data curation, writing, visualization, project administration. G.X., A.P., D.S.G.., S.C., D.S.N, B.G.: Methodology, validation, formal analysis, data curation. A.W.Y., K.S.C., A.S.: Formal analysis, data curation, visualization, methodology. J.A.P.: Methodology, validation, formal analysis, software, data curation. J.Q.: Resources. J.L.H: data curation, resources. D.J.K.: methodology, investigation, analysis, data curation, resources, manuscript editing. Y.W.: Methodology, validation, formal analysis, investigation, data curation, supervision, conceptualization- cell line screening efforts, manuscript editing, project administration, funding acquisition. D.G.H: resources, supervision, funding acquisition. C.K.: Conceptualization, methodology, investigation, resources, data curation, writing, visualization, supervision, project administration, funding acquisition.

Figure Legends

Figure 1. ARID1A/ARID1B dual-deficient endometrial tumors exhibit cBAF loss and increased abundance of ncBAF and PBAF complex components. A. Pie chart reflecting targeted sequence profiling of mSWI/SNF-mutated dedifferentiated endometrial and ovarian carcinomas (DFCI and Coatham et al., 2016 cohorts) indicating mutational frequencies of mSWI/SNF genes. Dual ARID1A and ARID1B mutations are present in ~33% of DDEC cases. B. Schematic highlighting n=3 ARID1A/B-intact, ARID1A-loss and ARID1A/B-dual-loss endometrioid cancer cell lines used in this study. C. Immunoblot for selected mSWI/SNF subunits spanning all 3 complex types performed on nuclear extracts isolated

from ARID1A/B-intact, ARID1A-loss, and ARID1A/B dual-deficient endometrial cell lines. D. Quantitative densitometry analyses performed on immunoblots for ncBAF subunits (BRD9, GLTSCR1) and PBAF subunits (BRD7, ARID2) in ARID1A/B-intact, ARID1A-loss, and ARID1A/B dual-deficient endometrial cell lines. E. Density sedimentation studies using 10-30% glycerol gradients performed on nuclear extracts isolated from KLE and VOA1066 cell lines and immunoblotted for selected mSWI/SNF subunits. F. H&E and immunostaining for ARID1A, ARID1B, SMARCA4 and GLTSCR1 performed on representative DDEC cases, showing well-differentiated and undifferentiated compartments. G. Representative photomicrographs of DDEC, indicating well-differentiated and dedifferentiated compartments; number of cases used in analyses are indicated. H. Bar graph quantifying GLTSCR1 staining intensity in DDEC well-differentiated and undifferentiated compartments. *; $p<0.03$, two-tailed t-test. Bars represent s.e.m.

Figure 2. cBAF reassembly controls genome-wide redistribution of mSWI/SNF family complexes in DDEC cells. A. Schematic for overexpression of HA-tagged full-length ARID1A in AN3CA and VOA1066 cell lines using an inducible piggyBac system. B. Immunoblot for mSWI/SNF complex components spanning cBAF (ARID1A), PBAF (ARID2) and ncBAF (GLTSCR1, BRD9), along with TBP as loading control in both AN3CA and VOA1066 cell line systems in (-) and (+) Dox conditions. C. Density sedimentation analyses performed on AN3CA ARID1A/B dual-deficient cells in -Dox (control) and +Dox (ARID1A rescue) conditions using 10-30% glycerol gradients. Immunoblots for selected mSWI/SNF subunits are shown. D. Bar graphs depicting Log2FC in whole-cell mSWI/SNF subunit abundance in AN3CA and VOA1066 cells in -/+ Dox (ARID1A rescue) conditions defined by TMT mass-spectrometry (n=2 replicates per condition); significance scores are indicated in the legend; ncBAF- and PBAF-specific subunits are indicated in bold. E. Summed log-fold changes for peptides corresponding to cBAF, PBAF, and ncBAF subunits in VOA1066 and AN3CA cell lines upon ARID1A rescue (+Dox/-Dox logFC) shown as heatmap. F. Cell proliferation experiments in AN3CA and VOA1066 DDEC cell lines treated with either no Dox or Dox-mediated induction of ARID1A expression. n=5 experimental replicates; error bars represent s.d.; ** $p<0.01$, ***$p<0.001$. G. Heatmaps reflecting ChIP-seq in AN3CA cells for HA (ARID1A), SMARCA4, SS18, BRD9, GLTSCR1, PBRM1 and H3K27Ac (each normalized to input), along with ATAC-seq. Gained, lost and retained peak sets are indicated. H. HOMER motif analyses performed over gained and lost SMARCA4 sites in AN3CA; HOMER motif analyses performed over gained and lost SMARCA4 sites in AN3CA +Dox (ARID1A rescue) versus -Dox (control) I. Representative ChIP-seq tracks over the *KRT7*, and *CLDN2* loci in AN3CA cells. J. Venn diagrams depicting BRD9-GLTSCR1 (ncBAF) merged peaks in -/+Dox (ARID1A rescue) conditions in AN3CA and VOA1066 cell lines. K. Heatmaps depicting ATAC-seq signal along with BRD9 and GLTSCR1 ChIP-seq signal over gained, lost and retained ATAC-seq peaks in AN3CA cells. L. Representative ChIP-seq tracks for BRD9, GLTSCR1, and SMARCA4 over the *E2F2* and *KCNG4* loci in AN3CA cells.

Figure 3. ARID1A/ARID1B-mediated mSWI/SNF complex reshuffling underlies altered gene regulation in DDEC cell lines and primary tumors. A. Volcano plots showing up- (red) and down- (blue) regulated genes following 72 hours of ARID1A restoration in AN3CA and VOA1066 DDEC cell lines. B. Hallmark GSEA showing ARID1A rescue-mediated gene expression pathway changes in AN3CA and VOA1066 cells. C. Scatter plot depicting significantly changed proteins (x-axis, TMT mass-spec) and RNA levels (RNA-seq) following ARID1A rescue in AN3CA and VOA1066 cells (merged datasets). D. Pie charts reflecting downregulated genes that are primary targets (defined as BRD9/GLTSCR1 co-targeted genes) and secondary targets (not ncBAF-targeted) and upregulated genes that are targeted by cBAF (defined as HA/ARID1A co-targeted site) upon rescue of ARID1A in AN3CA and VOA1066 cells. E. (Left) Log2FC of cBAF occupancy, ATAC-seq, and RNA-seq signals upon ARID1A rescue; (right) Log2FC of ncBAF occupancy, ATAC-seq, and RNA-seq. F. Representative ChIP-seq and ATAC-seq tracks at the KRT7 and E2F2 loci with corresponding bar graphs depicting gene expression (RNA-seq). G. Schematic of experiments in AN3CA cells with rescue of either HA-tagged

ARID1A or ARID1B. H. Immunoblot for ARID1A, ARID1B and GAPDH performed on whole cell lysates from AN3CA cells in indicated conditions. I. Volcano plot indicating ARID1A- and ARID1B- specific upregulated genes. J. Venn diagrams indicating overlap of upregulated genes (left) and sites with increased accessibility (right) following ARID1A, ARID1B or ARID1A/B dual rescue (+Dox). K. Heatmaps depicting k-means clustered sites with ATAC-seq signal and RNA-seq signal shown as z-scores. L. Schematic depicting laser capture microdissection (LCM) performed on undifferentiated (UD) and well-differentiated (WD) components of primary human DDEC tumors. M. Genes significantly enriched in UD and WDprimary tumor components. N. Hallmark GSEA performed on UD- and WD-specific genes. O. GSEA (C2 gene set) performed on AN3CA and VOA1066 cells with +Dox ARID1A rescue (relative to control), WD compared to UD and normal endometrium compared to UD.

Figure 4. Dual ARID1 paralog-deficient DDEC cells are sensitive to genetic disruption of ncBAF and PBAF components. A. Immunoblot performed on whole-cell extracts from AN3CA cells treated with indicated shRNAs targeting BRD9 or ARID2. B. Bar graph depicting quantification of area covered in indicated conditions in AN3CA colony formation assays. C. Immunoblot performed on whole-cell extracts from HEC-50B cells and HEC1B cells treated with either non-targeting sgRNA or sgRNA targeting ARID1B (HEC1B ARID1B KO). D. Schematic for CRISPR screening experiments in HEC1B cells (naive (WT) and ARID1B KO conditions). E. Scatter plot indicating CRISPR screening score (RRA) in WT and ARID1B KO HEC1B cells. F. Dependencies in HEC1B WT specific (Blue), HEC1B ARID1B KO (red) and both (purple) displayed in log2FC RRA; significant top hits in each are indicated. G. GSEA performed on HEC1B WT cells and in HEC1B ARID1B KO conditions. H. Impact of ARID1A rescue in AN3CA and VOA1066 cell lines on top HEC1B ARID1B KO-specific dependency genes displayed as log2FC. I. Dependencies in HEC1B and ARID1B KO HEC1B cells overlapping with impact by mSWI/SNF ATPase inhibition (Cmp14 treatment) displayed as log2FC. J. Box and whisker plots indicating mean dependency scores (CRISPR gene effect) for BRD9, ARID2, and SMARCD1 across DepMap (Broad Institute) in endometrial cell lines with mutation conditions indicated.

Figure 5. Small molecule-mediated disruption of mSWI/SNF complexes attenuates oncogenic chromatin regulation and cell proliferation. A. Schematic for small molecule inhibition experiments in DDEC cell lines in culture. B. Cell proliferation measurements for VOA1066 cells upon treatment with either Cmp14 or dBRD9-A, compared to DMSO control. n=3 experimental replicates; Significance values are indicated. C. Volcano plots indicating up- (red) and down- (blue) regulated genes upon either Cmp14 or dBRD9-A treatment in VOA1066 cells; 72 hours treatment. D. GSEA performed on RNA-seq profiles in VOA1066 cells treated with Cmp14 and dBRD9-A, relative to DMSO. E. Venn diagram indicating overlap of downregulated genes (logFC>1; $p<0.01$) in Cmp14 and dBRD9-A conditions in VOA1066 cells. F. Representative ChIP-seq and ATAC-seq tracks at the SERPINE1 locus in VOA1066 cells and NUPR1 locus in AN3CA cells. G. (left) Heatmap indicating change in ATAC-seq signals in Cmp14 and dBRD9-A conditions (relative to DMSO control) in AN3CA cells; (right) gene expression change (z-score) from RNA-seq at corresponding loci. H. Top downregulated gene targets in AN3CA and VOA cell lines following Cmp14 or dBRD9-A treatment (relative to DMSO). Log2FC values are shown.

Figure 6. Pharmacologic disruption of residual mSWI/SNF complex activities attenuates DDEC tumor growth in vivo. A. Schematic depicting DDEC CDX and PDX tumor establishment and treatment with vehicle, Cmp14, or dBRD9-A in NRG mice. B. Tumor volume (mm^3) of XVOA14590 PDX model treated with either vehicle control, 20mg/kg IP Cmp14 (QD), or 50mg/kg IP dBRD9-A (QD). C. Tumor burden measurements for XVOA14590 PDX model treated with either vehicle control, Cmp14, or dBRD9-A. D. GSEA C2 pathway analysis performed on RNA-seq profiles (merged; n=5) in each treatment condition relative to vehicle control in XVOA14590 PDX model at day 16 (study endpoint). E.

Z-scored heatmap indicating concordantly upregulated (red) and downregulated (blue) genes in two DDEC cell lines, VOA1066 and AN3CA, and in PDX model XVOA14590 in vivo. Selected genes are labeled. F. Tumor burden measurements for VOA1066 CDX model treated with either vehicle or Cmp14. G. Relative luciferase units for VOA1066 luciferase-GFP expressing CDX model treated with either vehicle or FHD-286 over 25 day time course. H. Schematic representing CDX and PDX tumor establishment and treatment with vehicle, FHD-286 (1.5mg.kg, oral, QD), carboplatin (1.5mg/kg, IPI, weekly) and combination (FHD-286 and carboplatin) in NRG mice. I. Kaplan-Meier curves performed on VOA1066 CDXmodel (n=12 per condition) treated with either vehicle or FHD-286. J. Kaplan-Meier curve demonstrating survival of n=12 per condition for XVOA14590 treated with conditions indicated. *p-values *<0.05, ** <0.01, ***<0.001. p-values determined with two-tailed Students t-test for B,C, F and log rank test for G, I and H. Error bars represent mean +/- S.E.M.

Materials and Methods

Cell Lines

All female human cell lines (AN3CA, VOA 1066, KLE, HEC-265, HEC1A RL95-2, SNGM, HEC-50B and MFE-296 were grown at 37 °C in a humidified incubator with 5% CO_2. We cultured KLE and RL95-2 cell lines in DMEM:F12 (Gibco) supplemented with 10% Fetal Bovine Serum (FBS) (Gibco) with 0.005mg/mL insulin (Sigma-Aldrich) for RL95-2 only. HEC1A cells were grown in McCoy's 5A media (Gibco) with 10% FBS. For HEC-265 and HEC-50B cells, we used EMEM (Gibco) with 15% tetracycline-free FBS (Omega). SNGM cells were maintained in Ham's F12 (Gibco) with 20% FBS. Finally, VOA1066, AN3CA, and MFE-296 were cultured in EMEM (Gibco) with 15% tetracycline-free FBS (Omega). HEC1B were cultured in RPMI 1640 supplemented with 5% FBS. All cell lines were maintained in 100U/mL Penicillin-Streptomycin (Gibco).

Animal Models

All animal experiments adhered to the Canadian Council on Animal Care (CCAC) and Animals for Research Act (R.S.O. 1990, Chapter c. A.22) guidelines, with protocols approved by the University of British Columbia's Animal Care Committee (A17-0146, A22-005). Female NRG (NOD.Rag1KO.IL2RγcKO) mice (6-8 weeks old) were injected subcutaneously with either VOA1066 or VOA1066-Luciferase (luc) cells ($1x10^6$ cells/mouse) or PDX tumor cells (XVOA14590, 25mg/mouse), all in a 1:1 Matrigel (Corning) mixture (final volume 200 µl). Randomization to treatment groups occurred when average tumor volume reached predetermined benchmarks (100 mm^3 for VOA1066 xenografts, 75 mm^3 for XVOA14590 PDX in Cmp 14 and dBRD9a studies, 100 mm^3 for XVOA14590 PDX in FHD-286 +/- carboplatin study). For VOA1066-luc derived xenografts, ranking of bioluminescence from VOA1066-luc cells measured by IVIS machine 7-14 days post-inoculation guided randomization. Drugs were administered as follows: CPD-14 (20 mg/kg daily; oral for VOA1066 xenograft, intraperitoneal for XVOA14590 PDX; 6-on 1-off schedule) in 0.5% methylcellulose + 0.5% tween-80; dBRD9a (50 mg/kg daily, intraperitoneal, diluted in 10% HP-β-CD from a 100 mg/ml DMSO solution); FHD-286 (1.5 mg/kg daily, oral; 6-on 1-off for both VOA1066-luc and XVOA14590 xenografts) in 0.5% methylcellulose + 0.5% tween-80 (alone or with carboplatin); carboplatin (15 mg/kg weekly, intraperitoneal for VOA1066-Luc or 25 mg/kg weekly, intraperitoneal for XVOA14590). Tumor size were monitored 2-3 times weekly by caliper in all studies. Studies were terminated upon reaching humane endpoints or when average tumor volume in the vehicle-treated group reached 1500 mm^3 (single agent studies) or all individual tumors reached 1500 mm^3 (FHD-286 +/- carboplatin study). Tumor volume was calculated using the formula length x $width^2$ x 0.52. At study endpoint, tumors were dissected, weighed, and processed for either molecular analysis (snap frozen) or histology (fixed in 10% neutral buffered formalin).

Human tumor samples

Archival paraffin embedded tissue from selected patients with a diagnosis of dedifferentiated, undifferentiated or well differentiated endometrial cancer were obtained under institutional IRBs: 2022P001059 (DCFI) and H18-01652 (UBC). Diagnosis of DDEC/UDEC was established based on pathologic review by Brigham and Women's and Vancouver General Hospital's gynecologic pathology divisions. All DCFI cases with DNA sequencing data were previously sequenced and the data obtained under research IRB 2023P003629. Deidentified variables related to clinical outcomes extracted included sex, age, stage, treatment, progression free survival and overall survival are summarized in **Table S1**.

Plasmids, cloning and exogenous expression

For inducible expression, ARID1A and ARID1B coding sequences were cloned downstream of a doxycycline-inducible promoter in a piggybac vector. This vector also contains a separate Tet-On 3G cassette and a Blasticidin resistance gene separated by a P2A cleavage sequence, all driven by the human EF1a promoter. Sanger sequencing verified the accuracy of all constructs. Piggybac plasmids were co-transfected with a mammalian transposase expression plasmid into AN3CA cells using TransIT-T1 Transfection Reagent (Mirus Bio). Selection with 10 ug/ml Blasticidin for 5 days post-transfection enriched for stably transfected clones. Doxycycline treatment at 100 ng/ml for 72 hours induced expression of the transgene. A complete list of plasmids used in this study can be found in the STAR Methods section.

Isogenic AN3CA and VOA1066 cancer cell lines harboring knockouts (KO) of BRD9, GLTSCR1, GLTSCR1L, SMARCA4, and SMARCA2 were generated using a commercially available CRISPR/Cas9 KO plasmid system (Santa Cruz Biotechnology). Briefly, cells were seeded at 1.5 x 10^5 per well in 6-well plates with antibiotic-free media 24 hours before transfection. Transfection followed the manufacturer's protocol using 1 µg of each KO plasmid and UltraCruz transfection reagent (Santa Cruz). Following a 24-hour incubation, media was replaced with complete media containing antibiotics. At 72 hours post-transfection, GFP-positive cells, indicative of successful plasmid integration, were enriched by fluorescence-activated cell sorting. Sorted cells were pooled and expanded. Knockout of the target genes was confirmed by Western blot analysis demonstrating the absence of the corresponding proteins.

To generate inducible expression of short-hairpin RNA (shRNA) constructs targeting BRD9, ARID2 or a scrambled, non-silencing sequence were cloned downstream of a doxycycline-inducible promoter in a piggybac vector. This vector also contains a separate Tet-On 3G cassette and a Blasticidin resistance gene separated by a P2A cleavage sequence, all driven by the human EF1a promoter. Sanger sequencing verified the accuracy of all constructs. Piggybac plasmids were co-transfected with a mammalian transposase expression plasmid into AN3CA cells using the TransIT-T1 Transfection Reagent (Mirus Bio). Selection with 10 ug/ml Blasticidin for 5 days post-transfection enriched for stably transfected clones. Doxycycline treatment at 100 ng/ml for 72 hours induced expression of the transgene. All the sequences are in the STAR Methods section**.** Knockdown of the target genes was confirmed by Western blot analysis demonstrating a decrease of the corresponding proteins.

Nuclear Extraction

To isolate nuclear fractions, cells were harvested by trypsinization, followed by centrifugation at 1200 rpm for 5 minutes at 4°C. The resulting pellet was resuspended in 5 volumes of hypotonic buffer containing 50mM Tris pH 7.5, 0.1% NP-40, 1mM EDTA, 1mM $MgCl_2$, 100mM NaCl supplemented with protease inhibitors (PI) and phenylmethylsulfonyl fluoride (PMSF). After another centrifugation at 5,000 rpm for 5 minutes at 4°C, the supernatant containing cytosolic components was aspirated and the nuclear pellet was resuspended in double the pellet volume in EB300 buffer (50mM Tris pH 7.5, 0.1%

NP-40, 1mM EDTA, 1mM $MgCl_2$, 300mM NaCl) were vortexed then incubated on ice followed by centrifugation at 15,000 rpm for 10 minutes at 4°C the supernatant was recovered and kept at -80°C until use.

Western Blotting

Whole cell lysates were generated using RIPA lysis buffer (50mmol/L Tris, pH 8.0, 150mmol/L NaCl, 5mmol/L MgCl2, 1% Triton X-100, 0.5% sodium deoxycholate, 0.1% SDS) supplemented with protease and phosphatase inhibitor cocktail (#78440, Thermo Fisher). Nuclear extracts or whole cell lysates were resolved by sodium dodecyl sulfate-polyacrylamide gel electrophoresis (SDS-PAGE) using a precast 4%–12% Bis-Tris PAGE gel (Bolt 4%–12% Bis-Tris Protein Gel, Thermo Fisher Scientific) following the manufacturer's protocol. Proteins were then electrophoretically transferred to polyvinylidene difluoride (PVDF) membranes (0.2 µm, Bio-Rad) at 400 mA for 2 hours at 4°C. Membranes were blocked with 5% (w/v) nonfat dry milk in Tris-buffered saline with 0.1% Tween-20 (TBST) for 30 min at room temperature. Following blocking, membranes were incubated with primary antibodies diluted in TBST with shaking overnight at 4°C. The primary antibody concentration used was 1:1000 (v/v) for all antibodies. After incubation, membranes were washed three times with TBST. Membranes were then probed with species- specific near-infrared fluorophore-conjugated secondary antibodies (LI-COR Biosciences) at a 1:10,000 (v/v) dilution in TBST for 1 hour at room temperature with shaking. Membranes were washed twice with TBST followed by a final wash with Tris-buffered saline (TBS). Finally, protein bands were visualized and quantified using a Li-Cor Odyssey CLx imaging system (LI-COR Biosciences).

Density Sedimentation

Glycerol gradient sedimentation was performed as previously described[15]. Briefly, nuclear extracts were resuspended in EB300 buffer (50mM Tris pH 7.5, 1.0% NP-40, 1mM EDTA, 1 mM $MgCl_2$, 300m NaCl) supplemented with 1 mM DTT, protease inhibitors, and 1 mM PMSF, followed by quantification using BCA. For each sedimentation run, 1mg of total nuclear lysate was loaded on top of a linear 10%–30% glycerol gradients with BC0 as the base buffer. Glycerol gradient tubes were loaded into a SW41 rotor and centrifuged at 40,000 rpm for 16 hours at 4°C. Following centrifugation, sample was aliquoted in 550 µL fractions. 100-250 µL of each aliquoted fraction were concentrated using 10-15 µL Strataclean beads (Agilent) with constant rotation for 2h at 4°C. The protein-bound beads were eluted in fresh sample buffer (2×NuPAGE LDS buffer with 100mM DTT) and loaded onto 4–12%Bis-Tris NuPAGE Gels (Life Technologies).

Tissue microarray construction and Immunohistochemistry

A collection of DDEC patient tumors was obtained from Vancouver General Hospital (VGH) with the study approval by the Institutional Review Board (IRB) at the University of British Columbia IRB# H18-01652 and from Brigham and Women's Hospital (BWH) IRB# P001059. Informed consent was obtained or waived from all participants in accordance with the relevant IRB approvals. For the VGH samples following histologic review of hematoxylin and eosin (H&E) slides previously prepared for clinical use by gynecologic pathologists, duplicate 0.6 mm cores of undifferentiated and well differentiated components from formalin-fixed, paraffin-embedded tumor tissue of each case were used for tissue microarray (TMA) construction. Each TMA section was cut at 4 µm thickness onto Superfrost Plus glass slides and were processed using the Leica BOND RX Stainer. For all cases from VGH and BWH, immunohistochemical staining was performed on 4 µm formalin-fixed paraffin embedded sections with antibodies to 1:3000 ARID1A (Cat# ab182560; RRID: AB_2889973) or 1:500 ARID1A (Cat# H00057492-M01J; RRID: AB_605947) , 1:250 ARID1B (Cat# H00057492-M01J; RRID: AB_605947), 1:2000 SMARCA4 (Cat# ab108318; RRID: AB_10889900), 1:200 SMARCA2 (Cat# HPA029981;

RRID:AB_10602406), 1:1000 SMARCB1 (Cat# 612110; RRID: AB_399481) and 1:500 GLTSCR1 (Cat# 45441; RRID: AB_3095741). IHC staining was reviewed and scored by DK. ARID1A, ARID1B, SMARCA4, SMARCA2, and SMARCB1 were interpreted as either intact/normal if staining was present in tumor nuclei or lost/aberrant if tumor nuclei showed an absence of staining. For dedifferentiated carcinomas, ARID1A, ARID1B, SMARCA4, SMARCA2, SMARCB1 were assessed in the undifferentiated component. Appropriate internal controls showed positive staining. GLTSCR1 staining was semi-quantitatively assessed using the method described previously.[49]

Immunofluorescence staining

VOA1066 and AN3CA cells were seeded onto sterile glass coverslips at the bottom of 6-well plates (Corning) at a density that achieved 75% confluency 72 hours after plating. To induce ARID1A expression, doxycycline (Fisher Scientific) was added to the culture medium at a final concentration of 100 ng/mL. After 72 hours, cells were washed twice with PBS followed by fixation with 3% paraformaldehyde for 20 minutes at room temperature. Cells were then permeabilized and blocked by incubation with Wash buffer (PBS containing 0.1% NP-40, 1 mM sodium azide, and 10% FBS) for 1 hour at room temperature. Pan Cytokeratin (AE1/AE3) Alexa Fluor 488 (Cat# 53-9003-82; RRID: AB_1834350) was diluted 1:200 in Wash buffer and incubated overnight at 4°C. Following incubation, cells were washed five times with Wash buffer. Finally, coverslips were mounted onto glass slides using InvitrogenProLong Gold Antifade Mountant (Fisher Scientific).

ATAC-Sequencing

DNA accessibility was measured using a modified Omni-ATAC protocol.45Briefly, 100,000 cells per sample were trypsinized and washed with cold PBS to remove trypsin. Cell pellets were lysed in 50 µL cold resuspension buffer (RSB) supplemented with fresh NP40 (final 0.1% v/v), Tween-20 (final 0.1% v/v), and Digitonin (final 0.01% v/v) (RSB recipe: 10 mM Tris-HCl pH 7.4, 10 mM NaCl, and 3 mM MgCl2). The lysis step was quenched with 1 mL of RSB supplemented with Tween-20 (final 0.1% v/v), and nuclei were pelleted at 500 g for 10 min at 4 °C after incubating on ice for 3 minutes. Nuclei were then resuspended in 50 µL transposition reaction mix containing 25 µL 2X Tagment DNA buffer (Illumina), 2.5 µL Tn5 transposase (Illumina), 16.5 µL 1X PBS, 0.5 µL 1% digitonin (final 0.01% v/v), 0.5 µL 10% Tween-20 (final 0.1% v/v), and 5 µL of nuclease-free water. The transposition reaction was carried out at 37 °C for 30 min with constant shaking (1000 rpm) on a thermomixer. Tagmented DNA was purified using the MinElute Reaction Cleanup Kit (Qiagen). Standard ATAC-seq amplification protocol with 7 cycles of amplification was used to amplify tagmented libraries.46Libraries were sequenced on a NextSeq 500 (Illumina) using 37 bp paired-end sequencing.

RNA-Sequencing

For bulk cell line RNA sequencing, total RNA was isolated from two million cells per sample of AN3CA and VOA1066 cell lines; all experimental conditions were performed in triplicate. Cells were first collected and washed with cold PBS to remove trypsin, then stored in RLT buffer (Qiagen) for subsequent RNA isolation. RNA purification was performed using the RNeasy kit (Qiagen) following the manufacturer's instructions. Next, RNA libraries were prepared using the Illumina NEBNext Ultra II Directional RNA Library Prep Kit. The quality and quantity of these libraries were assessed using a TapeStation (Agilent) and a Qubit Fluorometer (Thermo Fisher Scientific), respectively. Finally, the prepared RNA-seq libraries were sequenced on an Illumina NextSeq 500 platform using a single-end, 75-bp read length.

For RNA was extracted from FFPE tissue, RNAeasy FFPE kit (Qiagen) was used according to manufacturer's protocol. Briefly, samples obtained from laser capture microdissection were deparaffinized and lysed in a buffer containing proteinase K and on column DNAse treatment. The quality and quantity of RNA was assessed using a TapeStation (Agilent) and Qubit Fluorometer (Thermo Fisher Scientific). 100ng of purified RNA was used with the KAPA mRNA Hyperprep kit for library generation. Prepared RNA-seq libraries were sequenced on an Illumina Next-Seq instrument.

ChIP-Sequencing

Chromatin Immunoprecipitation (ChIP) was performed on 40 million fixed human cells. Briefly, cells were trypsinized, washed twice with PBS to remove trypsin, and then divided into aliquots. Cells were crosslinked with 1% formaldehyde for 10 minutes at 37°C with constant agitation. Crosslinking was quenched with glycine, and cells were washed with cold PBS before storage at -80°C in 10-million aliquots. Ten million cells were used per epitope for subsequent ChIPs. Following nuclei isolation, chromatin was sheared to a desired size range using a Covaris E220 sonicator. Sonicated chromatin was clarified by centrifugation, and the supernatant was incubated overnight at 4°C with specific antibodies (2–3 µg) (see antibody list). Protein G Dynabeads were used to capture antibody-chromatin complexes, which were then washed extensively. Beads were eluted, and the eluate was treated with RNase A and Proteinase K to remove RNA and proteins, respectively. Purified ChIP DNA was isolated using SPRI beads, washed, and eluted in low-TE buffer for storage at -20°C. ChIP DNA libraries were prepared using the Illumina NEBNext Ultra II DNA Library Prep Kit following the manufacturer's instructions. Finally, all libraries were sequenced using single-end 75bp reads on the Illumina NextSeq 500 platform.

Laser Capture Microdissection and RNA sequencing from primary tumor specimens

For the isolation of well and dedifferentiated cancer components, laser capture microdissection (LCM) was employed. Briefly, tissue sections (5 µm) were cut from fixed paraffin embedded tissue blocks and mounted on CapSure LCM Film (Thermo Fischer). Paraffin-embedded sections were deparaffinized and rehydrated before H&E staining as follows. Briefly, slides were fixed in xylene for two minutes, graded ethanol from 100-75% for a total of three minutes, water for 2 minutes, hematoxylin for 2 minutes, water for 2 minutes, graded ethanol for 3 minutes and xylene for 1 minute then air-dried. Under a microscope integrated with the LCM system (Leica Microsystems), tumor cells were identified based on regions selected on hematoxylin and eosin slides with a goal of 5,000 cells per sample. Subsequently, a laser beam was used to precisely dissect the desired regions of interest, capturing the isolated cancer cells onto the CapSure film subjected to RNA isolation.

Drug treatments for cell proliferation and genomics assays

To induce expression of ARID1A or ARID1B transgenes AN3CA and VOA1066 cells were grown in MEM media either supplemented with 200ng/mL Doxycycline to induce expression for 72 hours before harvesting for ATAC-seq, ChIP-seq and RNA-seq. For drug treatment studies, AN3CA and VOA1066 cells were treated with DMSO, 750nM Compound 14 or 1µM dBRD9a for 72 hours before harvesting for ATAC-seq, ChIP-seq and RNA-seq (see Methods below).

Cell growth and viability assays

Cell viability assays and dose-response curves were performed for VOA1066, RL-952, SNGM, and AN3CA cell lines in 96-well plates with three technical replicates per condition. For proliferation assays, cells were seeded at 500 cells per well and treated for 6 days with drugs suspended in DMSO. The drug-containing media was replaced every 3 days with fresh media containing the corresponding drug concentration. Following the treatment period, cell viability was measured using a fluorescence-based viability assay, CellTiter-Glo® (Promega). Synergy between drugs was evaluated using the Combenefit software as previously described. Cells were plated in a 6x6 drug concentration matrix format in triplicate and viability was measured after 6 days using CellTiter-Glo® (Promega). Bliss synergy scores were calculated for each drug combination and mapped relative to cell proliferation using Combenefit v2.021. Colony formation assays were performed in 6-well plates. 1,000 cells per well were seeded and treated with 100 ng/mL doxycycline or indicated drugs for 14 days. After treatment, cells were washed with PBS, fixed with 4% paraformaldehyde, and stained with Crystal Violet solution (Sigma Aldrich).

HEC1B and HEC1B.KO CRISPR screen

HEC1B cells were transiently transfected with a pool of 3 GFP-tagged CRISPR/Cas9 KO plasmids targeting ARID1B (Santa Cruz, sc-402365). GFP-positive cells were sorted out for clonal expansion and screen of ARID1B knockout clones. To perform genome-wide dropout screen, Both HEC1B and an ARID1B knockout clone (HEC1B.BKO) cells were infected with TKOv3 genome-wide library (Addgene, #90294; PMID: 28655737) at a transduction efficiency of 30% aiming 500 times representation of each sgRNA. Cells were selected with puromycin for two days and 25x10^6 cells collected as a baseline. Remaining cells were kept in culture for 18 days post-infection and collected as the endpoint. Genomic DNA was isolated using QIAamp DNA Blood Maxi Kit following manufacturer's instructions. sgRNA library was amplified from genomic DNA using Illumina-compatible index primers and sequenced by NovaSeq platform aiming for 300-500 times read coverage. The sequencing data was analyzed statistically using the MAGeCK software to identify dependencies.[50]

Tandem Mass Tag (TMT)- Mass Spectrometry Data Analysis

Differential abundance analysis was performed on normalized protein counts using edgeR's glmFit and glmLRT functions (Figure 3C, S3G). Obtained log fold-change values and adjusted p-values were visualized using ggplot2. Log2FC values were calculated based on normalized protein counts and were plotted in Figures 2D,E and S2D.

RNA-seq Data Analysis

RNA-Seq reads were demultiplexed using bcl2fastq v2.20.0.422 aligned to the hg19 genome with STAR v2.5.2b.[51] Upregulated and downregulated genes were determined using DESeq2 (log2FC = 1, B-H p-value = 0.05).[52] DESeq2's estimateSizeFactors function was used to generate normalized counts. ggplot2[53] was used to generate volcano plots for changes in expression visualized as scatter plots. The eulerr R package[54] was used to generate venn diagrams of differential genes. Variance stabilizing transformed counts were used to generate PCA plots across the top 500 genes and plotted using ggplot2[55]. ComplexHeatmap R package[56] was used to generate heatmaps and visualize Z-Score normalized read counts for each gene across all conditions for each cell line. The Kendall and Spearman distance functions were used to perform hierarchical clustering in heatmaps. clusterProfiler GSEA function[57] was used through the msigdbr R package to perform GSEA analysis using the Hallmark and C2 gene sets. The "stat" output from DESeq2 was used to determine Differential expression ranking. For GSEA analysis in Fig S3D, GSEA software was obtained from the Gene Set Enrichment Analysis website [http://www.broad.mit.edu/gsea/downloads.jsp].

ATAC-seq Data Analysis

ATAC-seq reads were first trimmed using Trimmomatic v0.36, aligned with Bowtie2 v2.2.9, and filtered with Picard v2.8.0 (MarkDuplicates REMOVE_DUPLICATES=true) and SAMtools v 0.1.19 (-F 256 -f 2 -q 30). Reads mapping to regions defined in the ENCODE project's wgEncodeDacMapabilityConcensusExcludeable bed file were removed using bedtools v2.30.0. ATAC-seq data was processed by merging technical replicates using SAMtools merge. Peaks were called using MACS3 (-f BAMPE -g hs -q 0.001 --nomodel --extsize 200 –broad).

Differential accessibility was determined by calculating reads-per-million values across a merged set of peaks for a given comparison set, and using an RPM fold-change cutoff of 1.5. Differential accessibility was then visualized with venn diagrams generated using eulerr and PCA plots were generated using bedtools intersect using DESeq2. bedtools intersect was used to determine counts, then variance stabilizing transformation was applied. Site centers with flanking windows of 200bp (total window size of 400bp) were identified across given FASTA sequence sites. Motif enrichment across these sets of sites was determined using HOMER findMotifsGenome.pl against genone-background (-size 400). Barplots were generated to visualize HOMER motif results using ggplot2. Heatmaps and deepTools computeMatrix as used to generate metaplots over indicated peaks. deepTools bamCoverage (--binSize "40" --normalizeUsing "CPM" --exactScaling) was used to generate bigwig inputs for heatmaps. bedtools closest was used to assign different sets of sites to their nearest protein-coding gene, as annotated in Gencode Release 44. Stacked bar charts generated with ggplot in R to highlight distance to TSS highlighting the proportion of promotor, promoter proximal and distal enhancer regions.

ChIP-seq Data Analysis

ChIP-seq reads were aligned in a manner identical to ATAC-seq reads. Peaks were generated with MACS2 (AN3 CA: -f BAM -g hs –broad –broad-cutoff 0.01 --nomodel --extsize 150, VOA1066: -f BAM -g hs -q 0.001 --nomodel) Differential binding was determined using bedtools intersect and visualized using matplotlib. Tracks were generated using deepTools bamCoverage (--binSize "40" --normalizeUsing "CPM" --exactScaling).

FASTA sequences across these sets of sites were generated using site centers with flanking windows of 200bp (total window size of 400bp). Enriched motifs across these sets of sites were determined using HOMER findMotifsGenome.pl against genome-background (-size 400). HOMER motif known results were visualized as barplots using matplotlib. The Metascape web server was used to assess the enrichment of different pathways and gene sets using an input gene list. These gene lists were determined by up and downregulated genes across the indicated conditions, and the overlap of these deregulated genes with coordinated or anti-coordinated changes in accessibility and BAF localization (using genes assigned to changing peaks by nearest distance to TSS) as indicated in the figures. The significance of enriched pathways and gene sets were visualized as horizontal bar charts using the description column of the metascape_results.xlsx files. To elaborate, sites of interest were annotated to their nearest protein-coding gene against the hg19 refFlat gene annotation and distance to transcription start site (TSS) were calculated with a custom perl script. Gene intersections with gene subsets were visualized as volcano plots of logFC vs -log(adj.p). Gene intersections were input into downstream gene enrichment analysis such as Metascape with default parameters. Gene enrichment results from Metascape were visualized as barplots of -log(p-val) by each enriched term, process, or pathway as horizontal bar charts using matplotlib. RPKMs of different genes were visualized as bar plots across the indicated conditions using matplotlib or ggplot in R.

Different sets of sites were assigned to their nearest protein-coding gene using distances to TSS. These distances were visualized as stacked bar charts using ggplot in R, highlighting the proportion of promoter, promoter proximal, and distal enhancer regions.

Enrichment and Statistical Analyses

GraphPad Prism 8 software was used to generate graphs and statistical analysis. Statistical significance was determined by Student's t-test, one- and two-way ANOVA and log-rank test as appropriate. All experiments have been repeated in at least two independent experiments (n=2 biologic replicates). All immunoblots are representations of independent experiments.

Sequencing data information

All sequencing raw and processed data are made available in the Gene Expression Omnibus (GEO) database under the series GSE268960; http://www.ncbi.nlm.nih.gov/geo/query/acc.cgi?acc=GSE268960. Token for reviewer access is ohoxeaoalxupnev.

Supplemental Table Titles and Legends.

Table S1. Data and calculations for all TCGA, DFCI, MSKCC endometrial carcinoma cases used in IHC.

Table S2. Features of DDEC cell lines used in the study.

Table S3. TMT Mass spectrometric analysis for AN3CA and VOA DDEC cell lines -/+ ARID1A WT rescue (+Dox).

Table S4. Clinicopathological information of patients used in LCM experiments with RNA-seq.

Table S5. CRISPR screening raw data in HEC1B and HEC1B ARID1B KO cells.

References

1. Valencia, A. M. & Kadoch, C. Chromatin regulatory mechanisms and therapeutic opportunities in cancer. *Nat. Cell Biol.* **21**, 152–161 (2019).
2. Dawson, M. A. & Kouzarides, T. Cancer epigenetics: from mechanism to therapy. *Cell* **150**, 12–27 (2012).
3. Valencia, A. M. *et al.* Landscape of mSWI/SNF chromatin remodeling complex perturbations in neurodevelopmental disorders. *Nat. Genet.* **55**, 1400–1412 (2023).
4. Kadoch, C. Diverse compositions and functions of chromatin remodeling machines in cancer. *Sci. Transl. Med.* **11**, (2019).
5. Kadoch, C. & Crabtree, G. R. Mammalian SWI/SNF chromatin remodeling complexes and cancer: Mechanistic insights gained from human genomics. *Sci Adv* **1**, e1500447 (2015).
6. Santen, G. W. E. *et al.* Coffin-Siris syndrome and the BAF complex: genotype-phenotype study in 63 patients. *Hum. Mutat.* **34**, 1519–1528 (2013).
7. Chen, C.-A. *et al.* Retrospective analysis of a clinical exome sequencing cohort reveals the mutational spectrum and identifies candidate disease-associated loci for BAFopathies. *Genet. Med.* **24**, 364–373 (2022).
8. Versteege, I. *et al.* Truncating mutations of hSNF5/INI1 in aggressive paediatric cancer. *Nature* **394**, 203–206 (1998).
9. Kadoch, C. & Crabtree, G. R. Reversible disruption of mSWI/SNF (BAF) complexes by the SS18-SSX oncogenic fusion in synovial sarcoma. *Cell* **153**, 71–85 (2013).
10. Santen, G. W. E. *et al.* Mutations in SWI/SNF chromatin remodeling complex gene ARID1B cause Coffin-Siris syndrome. *Nat. Genet.* **44**, 379–380 (2012).
11. Tsurusaki, Y. *et al.* Mutations affecting components of the SWI/SNF complex cause Coffin-Siris syndrome. *Nat. Genet.* **44**, 376–378 (2012).
12. Ramos, P. *et al.* Small cell carcinoma of the ovary, hypercalcemic type, displays frequent inactivating germline and somatic mutations in SMARCA4. *Nat. Genet.* **46**, 427–429 (2014).
13. Pan, J. *et al.* The ATPase module of mammalian SWI/SNF family complexes mediates subcomplex identity and catalytic activity-independent genomic targeting. *Nat. Genet.* **51**, 618–626 (2019).
14. Valencia, A. M. *et al.* Recurrent SMARCB1 Mutations Reveal a Nucleosome Acidic Patch Interaction Site That Potentiates mSWI/SNF Complex Chromatin Remodeling. *Cell* **179**, 1342–1356.e23 (2019).
15. Mashtalir, N. *et al.* Modular Organization and Assembly of SWI/SNF Family Chromatin Remodeling Complexes. *Cell* **175**, 1272–1288.e20 (2018).
16. Mashtalir, N. *et al.* A Structural Model of the Endogenous Human BAF Complex Informs Disease Mechanisms. *Cell* **183**, 802–817.e24 (2020).
17. Michel, B. C. *et al.* A non-canonical SWI/SNF complex is a synthetic lethal target in cancers driven by BAF complex perturbation. *Nat. Cell Biol.* **20**, 1410–1420 (2018).
18. St Pierre, R. *et al.* SMARCE1 deficiency generates a targetable mSWI/SNF dependency in clear cell meningioma. *Nat. Genet.* **54**, 861–873 (2022).
19. Tessier-Cloutier, B. *et al.* SWI/SNF-deficiency defines highly aggressive undifferentiated endometrial carcinoma. *Hip Int.* **7**, 144–153 (2021).
20. Silva, E. G., Deavers, M. T., Bodurka, D. C. & Malpica, A. Association of low-grade endometrioid carcinoma of the uterus and ovary with undifferentiated carcinoma: a new type of dedifferentiated carcinoma? *Int. J. Gynecol. Pathol.* **25**, 52–58 (2006).
21. Santoro, A. *et al.* Clinico-pathological significance of TCGA classification and SWI/SNF proteins expression in undifferentiated/dedifferentiated endometrial carcinoma: A possible prognostic risk stratification. *Gynecol. Oncol.* **161**, 629–635 (2021).
22. Coatham, M. *et al.* Concurrent ARID1A and ARID1B inactivation in endometrial and ovarian dedifferentiated carcinomas. *Mod. Pathol.* **29**, 1586–1593 (2016).

23. Hammer, P. M. *et al.* Molecular Classification Outperforms Histologic Classification in Prognostication of High-grade Endometrial Carcinomas With Undifferentiated and Sarcomatous Components. *Am. J. Surg. Pathol.* (2024) doi:10.1097/PAS.0000000000002250.
24. Travaglino, A. *et al.* TCGA Molecular Subgroups in Endometrial Undifferentiated/Dedifferentiated Carcinoma. *Pathol. Oncol. Res.* **26**, 1411–1416 (2020).
25. Cancer Genome Atlas Research Network *et al.* Integrated genomic characterization of endometrial carcinoma. *Nature* **497**, 67–73 (2013).
26. Ghandi, M. *et al.* Next-generation characterization of the Cancer Cell Line Encyclopedia. *Nature* **569**, 503–508 (2019).
27. Hnisz, D. *et al.* Super-enhancers in the control of cell identity and disease. *Cell* **155**, 934–947 (2013).
28. Wang, X. *et al.* SMARCB1-mediated SWI/SNF complex function is essential for enhancer regulation. *Nat. Genet.* **49**, 289–295 (2017).
29. Mathur, R. *et al.* ARID1A loss impairs enhancer-mediated gene regulation and drives colon cancer in mice. *Nat. Genet.* **49**, 296–302 (2017).
30. Kelso, T. W. R. *et al.* Chromatin accessibility underlies synthetic lethality of SWI/SNF subunits in ARID1A-mutant cancers. *Elife* **6**, (2017).
31. Papillon, J. P. N. *et al.* Discovery of Orally Active Inhibitors of Brahma Homolog (BRM)/SMARCA2 ATPase Activity for the Treatment of Brahma Related Gene 1 (BRG1)/SMARCA4-Mutant Cancers. *J. Med. Chem.* **61**, 10155–10172 (2018).
32. Remillard, D. *et al.* Degradation of the BAF Complex Factor BRD9 by Heterobifunctional Ligands. *Angew. Chem. Int. Ed Engl.* **56**, 5738–5743 (2017).
33. de Miguel, F. J. *et al.* Mammalian SWI/SNF chromatin remodeling complexes promote tyrosine kinase inhibitor resistance in EGFR-mutant lung cancer. *Cancer Cell* **41**, 1516–1534.e9 (2023).
34. Fiskus, W. *et al.* BRG1/BRM inhibitor targets AML stem cells and exerts superior preclinical efficacy combined with BET or menin inhibitor. *Blood* **143**, 2059–2072 (2024).
35. 1128P A phase I dose escalation and expansion study of FHD-286, a novel BRG1/BRM (SMARCA4/SMARCA2) inhibitor, for the treatment of metastatic uveal melanoma. *Paperpile* https://paperpile.com/app/p/7f4a5711-bb1a-0b1d-bbd8-2389e254ab56.
36. 1128P A phase I dose escalation and expansion study of FHD-286, a novel BRG1/BRM (SMARCA4/SMARCA2) inhibitor, for the treatment of metastatic uveal melanoma. *Paperpile* https://paperpile.com/app/p/7f4a5711-bb1a-0b1d-bbd8-2389e254ab56.
37. Eskander, R. N. *et al.* Pembrolizumab plus Chemotherapy in Advanced Endometrial Cancer. *N. Engl. J. Med.* **388**, 2159–2170 (2023).
38. Davis, J. M. *et al.* Long-term disease-free survival with chemotherapy and pembrolizumab in a patient with unmeasurable, advanced stage dedifferentiated endometrial carcinoma. *Gynecol Oncol Rep* **53**, 101380 (2024).
39. Wilson, M. R. *et al.* ARID1A and PI3-kinase pathway mutations in the endometrium drive epithelial transdifferentiation and collective invasion. *Nat. Commun.* **10**, 3554 (2019).
40. Suryo Rahmanto, Y. *et al.* Inactivation of Arid1a in the endometrium is associated with endometrioid tumorigenesis through transcriptional reprogramming. *Nat. Commun.* **11**, 2717 (2020).
41. Guan, B., Wang, T.-L. & Shih, I.-M. ARID1A, a factor that promotes formation of SWI/SNF-mediated chromatin remodeling, is a tumor suppressor in gynecologic cancers. *Cancer Res.* **71**, 6718–6727 (2011).
42. Reske, J. J. *et al.* SWI/SNF inactivation in the endometrial epithelium leads to loss of epithelial integrity. *Hum. Mol. Genet.* **29**, 3412–3430 (2020).
43. Nakayama, R. T. *et al.* SMARCB1 is required for widespread BAF complex-mediated activation of enhancers and bivalent promoters. *Nat. Genet.* **49**, 1613–1623 (2017).
44. Wang, Z. *et al.* Dual ARID1A/ARID1B loss leads to rapid carcinogenesis and disruptive redistribution of

BAF complexes. *Nat Cancer* **1**, 909–922 (2020).
45. Bailey, M. H. *et al.* Comprehensive Characterization of Cancer Driver Genes and Mutations. *Cell* **173**, 371–385.e18 (2018).
46. Cancer Genome Atlas Research Network. Comprehensive molecular characterization of gastric adenocarcinoma. *Nature* **513**, 202–209 (2014).
47. Zhang, Z. *et al.* Clinicopathological and prognostic significance of SWI/SNF complex subunits in undifferentiated gastric carcinoma. *World J. Surg. Oncol.* **20**, 383 (2022).
48. Tessier-Cloutier, B. *et al.* Loss of switch/sucrose non-fermenting complex protein expression in undifferentiated gastrointestinal and pancreatic carcinomas. *Histopathology* **77**, 46–54 (2020).
49. Crowe, A. R. & Yue, W. Semi-quantitative Determination of Protein Expression using Immunohistochemistry Staining and Analysis: An Integrated Protocol. *Bio Protoc* **9**, (2019).
50. Li, W. *et al.* MAGeCK enables robust identification of essential genes from genome-scale CRISPR/Cas9 knockout screens. *Genome Biol.* **15**, 554 (2014).
51. Dobin, A. *et al.* STAR: ultrafast universal RNA-seq aligner. *Bioinformatics* **29**, 15–21 (2013).
52. Love, M. I., Huber, W. & Anders, S. Moderated estimation of fold change and dispersion for RNA-seq data with DESeq2. *Genome Biol.* **15**, 550 (2014).
53. Wickham, H. *ggplot2: Elegant Graphics for Data Analysis*. (Springer Science & Business Media, 2009).
54. Quinlan, A. R. & Hall, I. M. BEDTools: a flexible suite of utilities for comparing genomic features. *Bioinformatics* **26**, 841–842 (2010).
55. Website. H, W. ggplot2: Elegant Graphics for Data Analysis. . Springer-Verlag New York. ISBN 978-3-319-24277-4, https://ggplot2.tidyverse.org. (2016).
56. Gu, Z., Eils, R. & Schlesner, M. Complex heatmaps reveal patterns and correlations in multidimensional genomic data. *Bioinformatics* **32**, 2847–2849 (2016).
57. Wu, T. *et al.* clusterProfiler 4.0: A universal enrichment tool for interpreting omics data. *Innovation (Camb)* **2**, 100141 (2021).

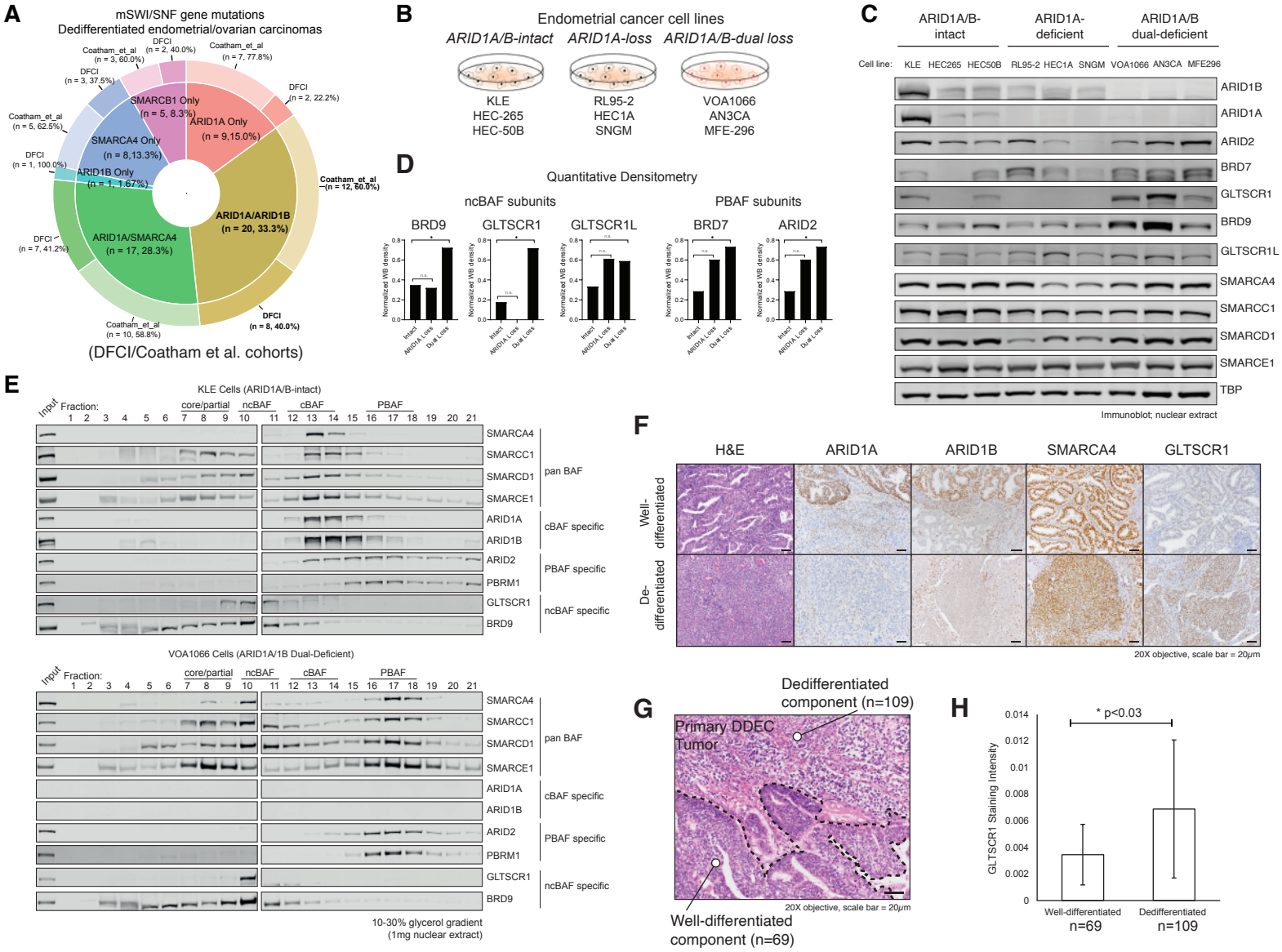

Figure 1. ARID1A/ARID1B dual-deficient endometrial tumors exhibit cBAF loss and increased abundance of ncBAF and PBAF complex components. A. Pie chart reflecting targeted sequencing of mSWI/SNF-mutant dedifferentiated endometrial, and ovarian carcinomas (DFCI and Coatham et al., 2016 cohorts) indicating mutational frequencies of mSWI/SNF genes. Dual ARID1A and ARID1B mutations are present in ~33% of DDEC cases. **B.** Schematic highlighting n=3 ARID1A/B-intact, ARID1A-loss and ARID1A/B-dual-loss endometrioid cancer cell lines used in this study. **C.** Immunoblot for selected mSWI/SNF subunits spanning all 3 complex types performed on nuclear extracts isolated from ARID1A/B-intact, ARID1A-loss, and ARID1A/B dual-deficient endometrial cell lines. **D.** Quantitative densitometry analyses performed on immunoblots for ncBAF subunits (BRD9, GLTSCR1) and PBAF subunits (BRD7, ARID2) in ARID1A/B-intact, ARID1A-loss, and ARID1A/B dual-deficient endometrial cell lines. **E.** Density sedimentation studies using 10-30% glycerol gradients performed on nuclear extracts isolated from KLE and VOA1066 cell lines and immunoblotted for selected mSWI/SNF subunits. **F.** H&E and immunostaining for ARID1A, ARID1B, SMARCA4 and GLTSCR1 performed on representative DDEC cases, showing well-differentiated and dedifferentiated compartments. **G.** Representative photomicrographs of DDEC, indicating well-differentiated and undifferentiated compartments; number of cases used in analyses are indicated. **H.** Bar graph quantifying GLTSCR1 staining intensity in DEC well-differentiated and undifferentiated compartments. *; p<0.03, two-tailed t-test. Bars represent s.e.m.

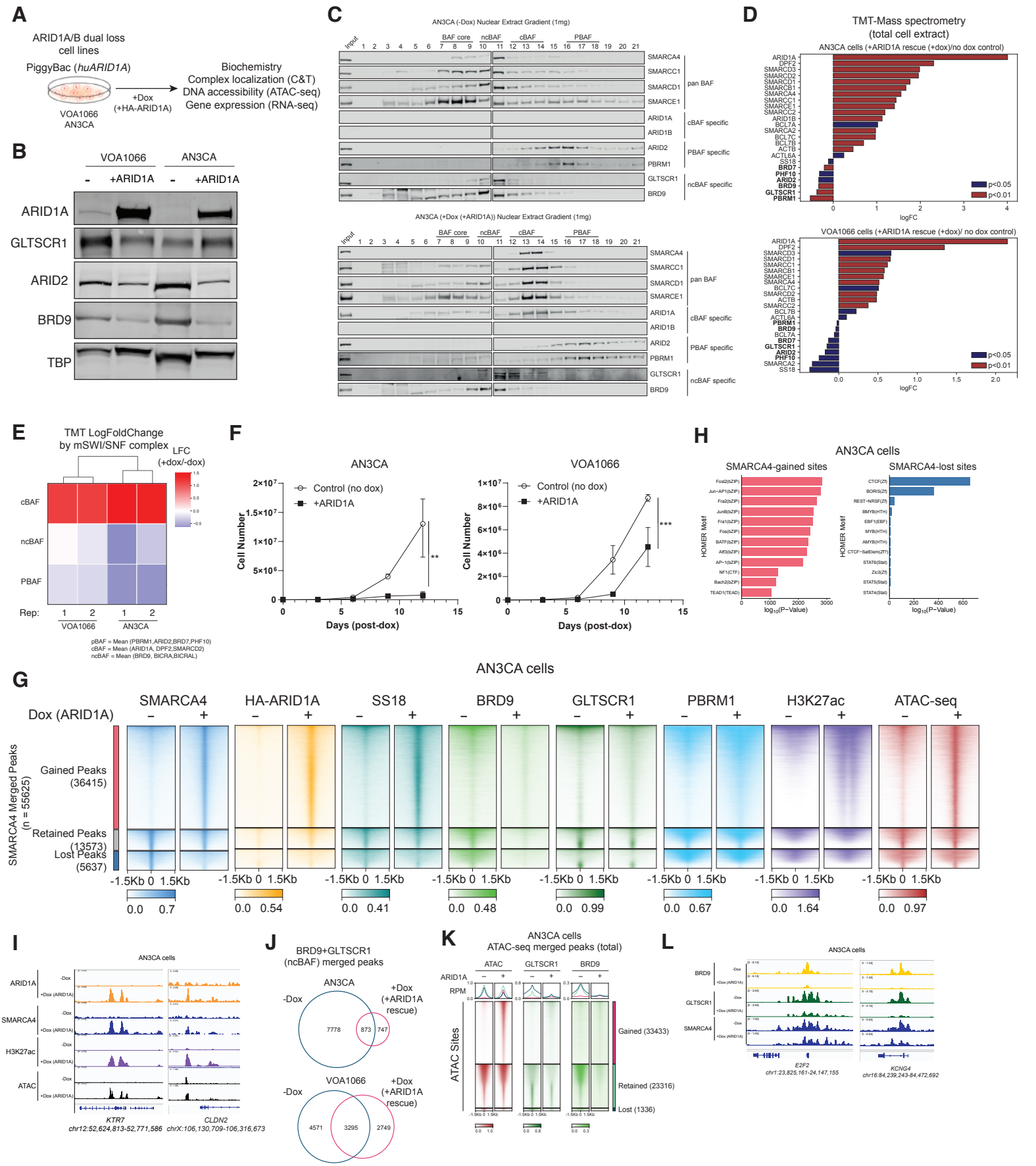

Figure 2. cBAF reassembly controls genome-wide redistribution of mSWI/SNF family complexes in DDEC cells.
A. Schematic for overexpression of HA-tagged full-length ARID1A in AN3CA and VOA1066 cell lines using an inducible piggyBac system. **B.** Immunoblot for mSWI/SNF complex components spanning cBAF (ARID1A), PBAF (ARID2) and ncBAF (GLTSCR1, BRD9), along with TBP as loading control in both AN3CA and VOA1066 cell line systems in (-) and (+) Dox conditions. **C.** Density sedimentation analyses performed on AN3CA ARID1A/B dual-deficient cells in -Dox (control) and +Dox (ARID1A rescue) conditions using 10-30% glycerol gradients. Immunoblots for selected mSWI/SNF subunits are shown. **D.** Bar graphs depicting Log2FC changes in whole-cell mSWI/SNF subunit abundance in AN3CA and VOA1066 cells in -/+ Dox (ARID1A rescue) conditions defined by TMT mass-spectrometry (n=2 replicates per condition); significance scores are indicated in the legend; ncBAF- and PBAF-specific subunits are indicated in bold. **E.** Summed log-fold changes for peptides corresponding to cBAF, PBAF, and ncBAF subunits in VOA1066 and AN3CA cell lines upon ARID1A rescue (+Dox/-Dox logFC) shown as heatmap. **F.** Cell proliferation experiments in AN3CA and VOA1066 DEC cell lines treated with either no Dox or Dox-mediated induction of ARID1A expression. n=5 experimental replicates; error bars represent s.d.; ** p<0.01, ***p<0.001. **G.** Heatmaps reflecting ChIP-seq in AN3CA cells for HA (ARID1A), SMARCA4, SS18, BRD9, GLTSCR1, PBRM1 and H3K27Ac (each normalized to input), along with ATAC-seq. Gained, lost and retained peak sets are indicated. **H.** HOMER motif analyses performed over gained and lost SMARCA4 sites in AN3CA;+Dox (ARID1A rescue), -Dox (no rescue control). **I.** Representative ChIP-seq tracks over the *KRT7*, and *CLDN2* loci in AN3CA cells. **J.** Venn diagrams depicting BRD9-GLTSCR1 (ncBAF) merged peaks in -/+ Dox (ARID1A rescue) conditions in AN3CA and VOA1066 cell lines. **K.** Heatmaps depicting ATAC-seq signal along with BRD9 and GLTSCR1 ChIP-seq signal over gained, lost and retained ATAC-seq peaks in AN3CA cells. **L.** Representative ChIP-seq tracks for BRD9, GLTSCR1, and SMARCA4 over the *E2F2* and *KCNG4* loci in AN3CA cells.

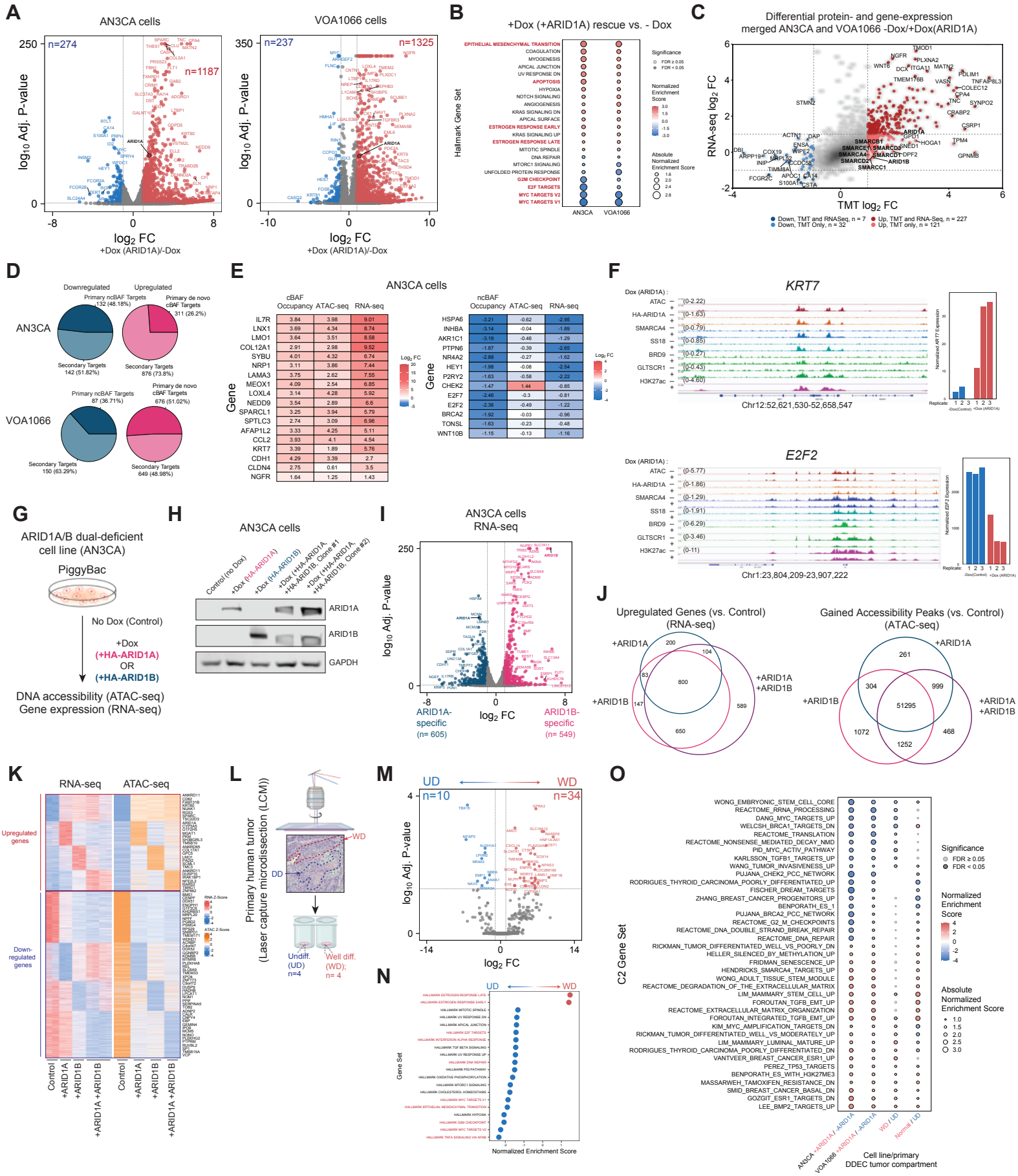

Figure 3. ARID1A/ARID1B-mediated mSWI/SNF complex reshuffling underlies altered gene regulation in DDEC cell lines and primary tumors.
A. Volcano plots showing up- (red) and down- (blue) regulated genes following 72 hours of +Dox (ARID1A restoration) in AN3CA and VOA1066 DDEC cell lines. **B.** Hallmark GSEA showing ARID1A rescue-mediated gene expression pathway changes in AN3CA and VOA1066 cells. **C.** Scatter plot depicting significantly changed proteins (x-axis, TMT mass-spec) and RNA levels (RNA-seq) following ARID1A rescue in AN3CA and VOA1066 cells (merged datasets). **D.** Pie charts reflecting downregulated genes that are primary targets (defined as BRD9/GLTSCR1 co-targeted genes) and secondary targets (not ncBAF-targeted) and upregulated genes that are targeted by cBAF (defined as HA/ARID1A co-targeted site) upon rescue of ARID1A in AN3CA and VOA1066 cells. **E.** (Left) Log2FC of cBAF occupancy, ATAC-seq, and RNA-seq signals upon ARID1A rescue; (right) Log2FC of ncBAF occupancy, ATAC-seq, and RNA-seq. **F.** Representative ChIP-seq and ATAC-seq tracks at the KRT7 and E2F2 loci with corresponding bar graphs depicting gene expression (RNA-seq). **G.** Schematic of experiments in AN3CA cells with rescue of either HA-tagged ARID1A or ARID1B (+Dox). **H.** Immunoblot for ARID1A, ARID1B and GAPDH performed on whole cell lysates from AN3CA cells in indicated conditions. **I.** Volcano plot indicating ARID1A- and ARID1B- specific upregulated genes. **J.** Venn diagrams indicating overlap of upregulated genes (left) and sites with increased accessibility (right) following ARID1A, ARID1B or ARID1A/B dual rescue (+Dox). **K.** Heatmaps depicting k-means clustered sites with ATAC-seq signal and RNA-seq signal shown as z-scores. **L.** Schematic depicting laser capture microdissection (LCM) performed on undifferentiated (UD) and well-differentiated (WD) sections of primary human endometrial tumors. **M.** Genes significantly enriched in UD and WD primary tumor components. **N.** Hallmark GSEA performed on UD- and WD-specific genes. O. GSEA (C2 gene set) performed on AN3CA and VOA1066 cells with +Dox ARID1A rescue (relative to control), WD compared to UD, and normal endometrium compared to UD.

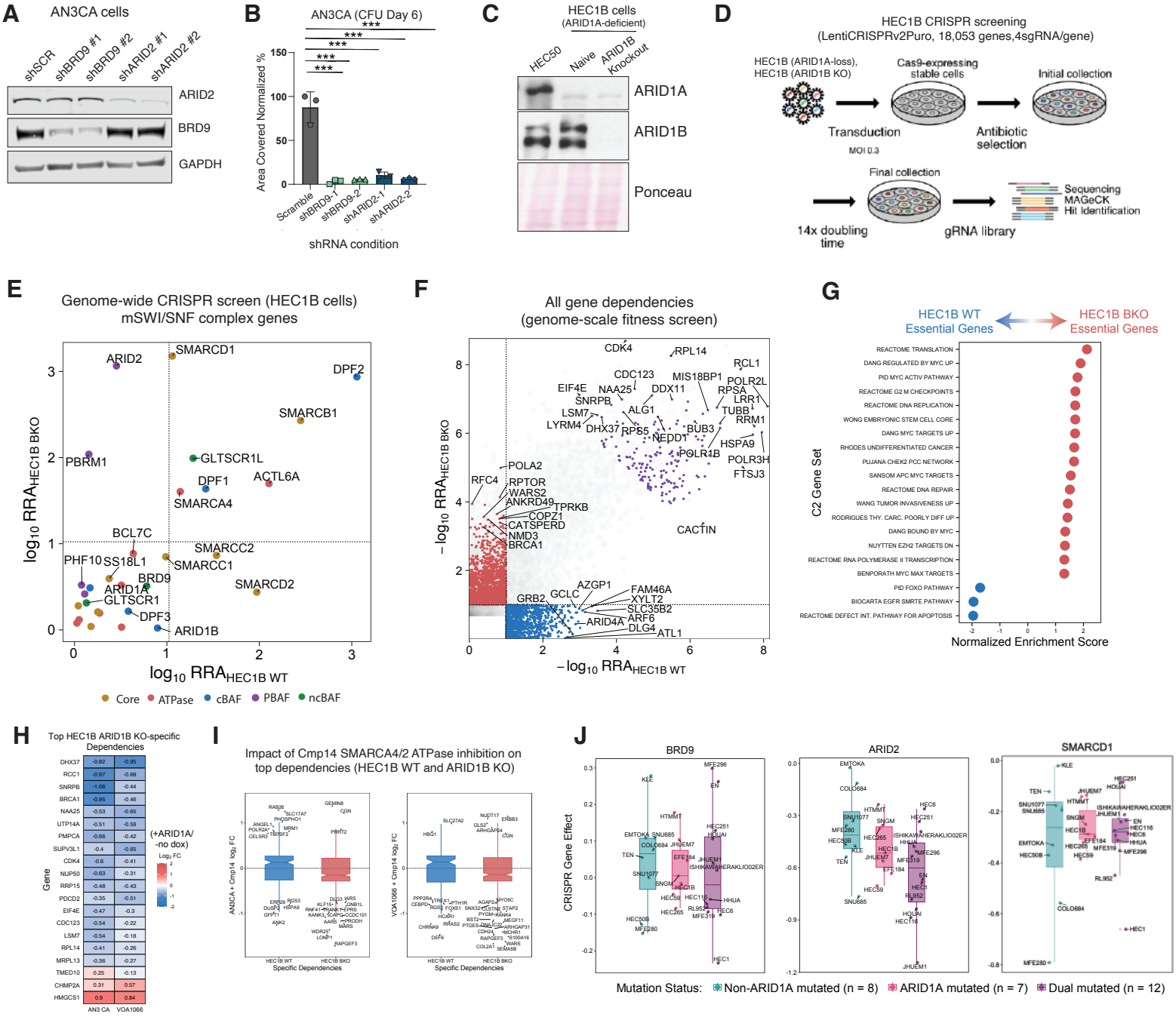

Figure 4. Dual ARID1 paralog-deficient DDEC cells are sensitive to genetic disruption of ncBAF and PBAF components.
A. Immunoblot performed on whole-cell extract from AN3CA cells treated with indicated shRNAs targeting BRD9 or ARID2. **B.** Bar graph depicting AUC values in indicated conditions in AN3CA colony formation assays. **C.** Immunoblot performed on whole-cell extracts from HEC-50B cells and HEC1B cells treated with either non-targeting sgRNA or sgRNA targeting ARID1B. **D.** Schematic for CRISPR screening experiments in HEC1B cells (naive and ARID1B KO conditions). **E.** Scatter plot indicating CRISPR screening score (RRA) in naive and ARID1B KO HEC1B cells. **F.** Dependencies specific to HEC1B WT (Blue), HEC1B ARID1B KO (red) and both cell conditions (purple) displayed in -log10 RRA; significant top hits in each are indicated. **G.** GSEA performed on HEC1B WT cells and in HEC1B ARID1B KO conditions. **H.** Impact of ARID1A rescue in AN3CA and VOA1066 cell lines on top HEC1B ARID1B KO-specific dependency genes displated as Log2FC. **I.** Dependencies in HEC1B and ARID1B KO HEC1B cells overlapping with impact by mSWI/SNF ATPase inhibition (Cmp14 treatment). **J.** Box and whisker plots indicating mean dependency scores (CRISPR gene effect) for BRD9, ARID2, and SMARCD1 across DepMap (Broad Institute) in endometrial cell lines with mutation conditions indicated in the legend.

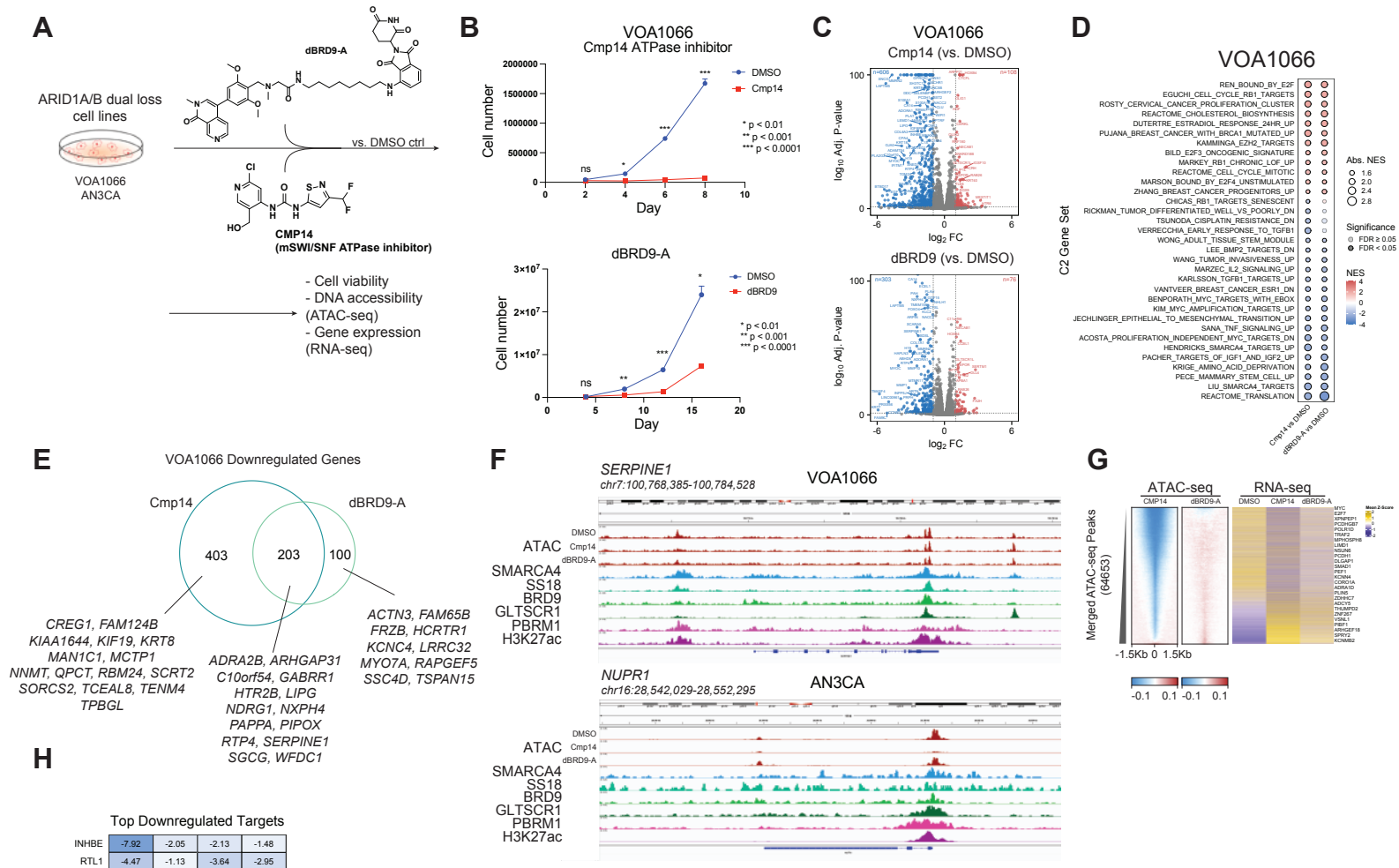

Gene	AN3CA Cmp14	AN3CA dBRD9-A	VOA1066 Cmp14	VOA1066 dBRD9-A
INHBE	-7.92	-2.05	-2.13	-1.48
RTL1	-4.47	-1.13	-3.64	-2.95
NUPR1	-6.29	-0.35	-2.83	-2.6
SERPINE1	-3.57	-1.28	-3.92	-2.33
P2RY6	-2.92	-0.97	-4.28	-2.53
MASP1	-6.01	-1.82	-1.36	-1.11
S100A1	-3.68	-1.09	-3.33	-1.75
CRYAB	-0.89	-0.27	-4.93	-2.83
CA14	-2.47	-1.06	-2.18	-2.59
LINC00523	-2.86	-1.18	-2.22	-1.64
GDF15	-5.28	-0.42	-0.93	-1.15
ASS1	-3.41	-0.74	-2.11	-1.47
S100A4	-2.59	-0.71	-3.35	-0.82
PRPH	-0.96	-0.34	-3.13	-2.68
NDUFA4L2	-1.97	-0.99	-2.17	-1.9
HAPLN3	-0.65	-1.24	-2.02	-3.1
WFDC1	-1.66	-0.88	-3.05	-1.08
EMP1	-1.6	-1.52	-1.08	-2.38
P2RX6	-1.23	-1.01	-2.1	-1.93
NXPH4	-0.79	-0.68	-2.54	-1.74

Figure 5. Small molecule-mediated disruption of mSWI/SNF complexes attenuates oncogenic chromatin regulation and cell proliferation.
A. Schematic for small molecule inhibition experiments in DDEC cell lines in culture. **B.** Cell proliferation measurements for VOA1066 cells upon treatment with either Cmp14 or dBRD9-A, compared to DMSO control. n=3 experimental replicates; Significance values are indicated. **C.** Volcano plots indicating up- (red) and down- (blue) regulated genes upon either Cmp14 or dBRD9-A treatment in VOA1066 cells; 72 hours treatment. **D.** GSEA performed on RNA-seq profiles in VOA1066 cells treated with Cmp14 and dBRD9-A, relative to DMSO. **E.** Venn diagram indicating overlap of downregulated genes (logFC>1; p<0.01) in Cmp14 and dBRD9-A conditions in VOA1066 cells. **F.** Representative ChIP-seq and ATAC-seq tracks at the SERPINE1 locus in VOA1066 cells and NUPR1 locus in AN3CA cells . **G.** (left) Heatmap indicating change in ATAC-seq signals in Cmp14 and dBRD9-A conditions relative to DMSO control in AN3CA cells; (right) gene expression change (z-score) from RNA-seq at corresponding loci. **H.** Top downregulated gene targets in AN3CA and VOA cell lines following Cmp14 or dBRD9-A treatment (relative to DMSO). Log2FC values are shown.

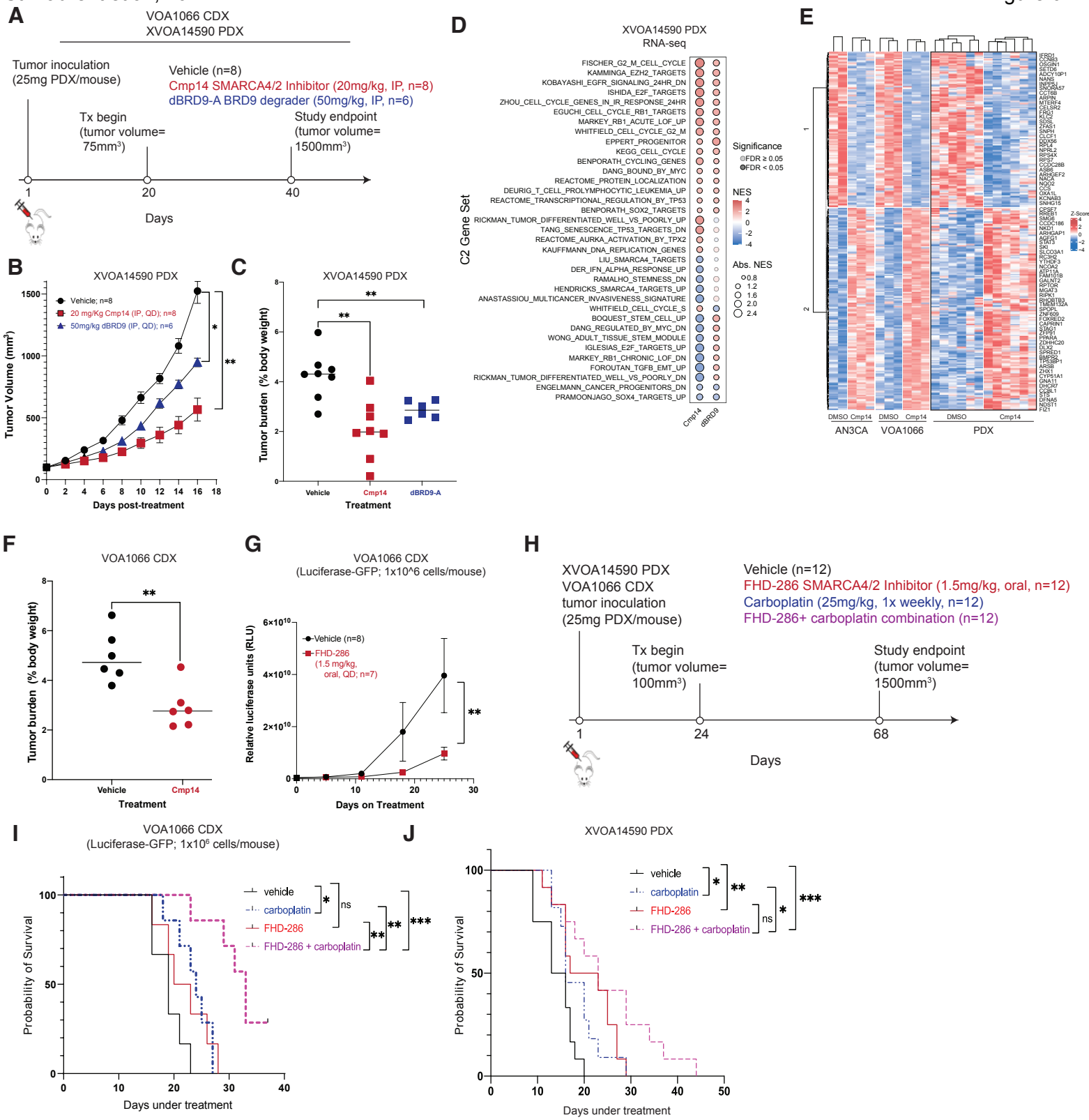

Figure 6. Pharmacologic disruption of residual mSWI/SNF complex activities attenuates DDEC tumor growth in vivo. **A.** Schematic depicting DDEC CDX and PDX tumor establishment and treatment with vehicle, Cmp14, or dBRD9-A in NRG mice. **B.** Tumor volume (mm³) of XVOA14590 PDX model treated with either vehicle control, 20mg/kg IP Cmp14 (QD), or 50mg/kg IP dBRD9-A (QD). **C.** Tumor burden measurements for XVOA14590 PDX model treated with either vehicle control, Cmp14, or dBRD9-A. **D.** GSEA C2 pathway analysis performed on RNA-seq profiles (merged; n=5) in each treatment condition relative to vehicle control in XVOA14590 PDX model at day 16 (study endpoint). **E.** Z-scored heatmap indicating concordantly upregulated (red) and downregulated (blue) genes in two DDEC cell lines, VOA1066 and AN3CA, and in PDX model XVOA14590 in vivo. Selected genes are labeled. **F.** Tumor burden measurements for VOA1066 CDX model treated with either vehicle or Cmp14. **G.** Relative luciferase units for VOA1066 luciferase-GFP expressing CDX model treated with either vehicle or FHD-286 over 25 day time course. **H.** Schematic representing CDX and PDX tumor establishment and treatment with vehicle, FHD-286 (1.5mg.kg, oral, QD), carboplatin (1.5mg/kg, IPl, weekly) and combination (FHD-286 and carboplatin) in NRG mice. **I.** Kaplan-Meier curves performed on VOA1066 cell line CDX model (n=12 per condition) treated with either vehicle or FHD-286. **J.** Kaplan-Meier curve demonstrating survival of n=12 per condition treated with conditions indicated. *p-values *<0.05, ** <0.01, ***<0.001. p-values determined with two-tailed Students t-test for B,C, F and log rank test for G, I and J. Error bars represent mean +/- S.E.M.